Journal of Nuclear Materials 569 (2022) 153918

Contents lists available at ScienceDirect

Journal of Nuclear Materials

journal homepage: www.elsevier.com/locate/jnucmat

Effect of irradiation swelling on the mechanical properties of unidirectional SiC/SiC composites: A numerical investigation at microstructural level

Yang Chen[a,b], James Marrow[a,*]

[a] Department of Materials, University of Oxford, Parks Road, Oxford OX1 3PH, UK
[b] Department of Mechanical Engineering, University of Bath, BA2 5AB, Claverton Down, UK

ARTICLE INFO

Article history:
Received 13 May 2022
Revised 5 July 2022
Accepted 13 July 2022
Available online 15 July 2022

Keywords:
SiC/SiC composite
Swelling mismatch
Damage
Residual stress
Numerical simulation

ABSTRACT

In order to apply SiC/SiC composites in nuclear systems, it is essential to understand the potential effects of dimensional changes induced by neutron irradiation on property degradation. A microscale model has been developed to predict the mechanical behaviour of irradiated fibre composites, including matrix cracking and interface debonding. The present work investigated the states of residual stresses and damage that may be induced by swelling mismatch between fibres and matrix, and their subsequent effects on the transverse and longitudinal tensile mechanical properties of composites. Unidirectional (UD) composites with various fibre contents and porosities were subject to different swelling mismatch to simulate irradiation-induced dimensional changes. The composites were then virtually tested in tension to determine the modulus and strength. The focus of the present work is the transverse properties, and some illustrative results for the longitudinal behaviour are also presented. The sensitivity of the composites' properties to irradiation swelling was affected by the fibre volume fraction, and not by the pore volume fraction, though the porosity dramatically affected the initial unirradiated properties. The model correctly describes experimental trends reported in the literature, and a simple optimisation of the model parameters is demonstrated by the successful simulation of experimental data for tensile loading of a mini composite specimen.

1. Introduction

Due to their unique properties under fast neutron irradiation and temperature [1,2], SiC/SiC composites are promising materials to fulfil the requirements for accident tolerant fuel cladding in light water nuclear reactors and advanced gas-cooled nuclear reactors [3,4]. In order to achieve a good tolerance to tensile strain, as required for fuel assembly and transport, one of the manufacturing strategies relies on a relatively large porosity (roughly around 10%) that remains after the chemical vapour infiltration (CVI) process. The porous SiC/SiC structure, together with the weak interphase, promotes a pseudo-ductile mechanical behaviour, which includes contributions from micro-cracking of local constituents. Although the nonlinear behaviour of porous SiC/SiC composites may be highly reproducible [5–9], for long-term safe application in nuclear plants it is essential to fully understand the interaction between fast neutron irradiation and the damage mechanisms, as this may affect the tolerance to mechanical loading. Numerous investigations of damage in the unirradiated condition have been performed, using experimental techniques such as acoustic emission [10], electric resistivity [11], surface digital image correlation [12] and X-ray computed tomography [7,13–15]. However, due to the difficulty in manipulating irradiated samples, and also their limited availability, the effects of neutron irradiation on the mechanical properties of SiC/SiC composites have been studied by a relatively limited number of works, mainly using macroscopic testing and post-mortem observations.

It is commonly accepted that the SiC matrix exhibits similar effects from neutron irradiation as high-purity β-phase SiC [1,3]. Within the temperature range of 150 °C ~ 1000 °C, the key irradiation effects are volumetric swelling, significant decrease in thermal conductivity and slight decrease in elastic modulus. These irradiation effects saturate at relatively low irradiation fluence, typically of the order of ~1 dpa (displacements per atom) [1]. In contrast to the SiC matrix, the number of investigations of the irradiation behaviours of SiC fibres and the PyC interphase is more limited. Nozawa et al. [16] reported that both neutron irradiation fluence and temperature (0.7 ~ 7.7 dpa and 380 °C ~ 1080 °C,

* Corresponding author.
E-mail address: james.marrow@materials.ox.ac.uk (J. Marrow).

https://doi.org/10.1016/j.jnucmat.2022.153918

respectively) induced "measurable yet not so dramatic" degradation in the shear strength of the PyC interphase, and the temperature dependence was minor at <1000 °C. They also compared the performance of monolayer PyC and multilayer PyC/SiC interphases, and showed that the multilayer interphase exhibited higher shear strength in both unirradiated and irradiated conditions. Their later study [17] showed that the thickness of the interphase (either monolayer or multilayer) might have a significant effect on the fibre/matrix debonding under irradiation, which was the major cause of the mechanical degradation of composites. Various works have compared the irradiation performance of composites based on different SiC fibres. Koyanagi et al. [18] measured the swelling of Tyranno SA3 (TSA) SiC fibres with both CVI and NITE (nano-infiltrated and transient eutectic phase) SiC matrices under ion irradiation (Si^{2+} ions to 3 dpa between 600 °C ~ 1000 °C), and found that the NITE SiC matrix exhibited a larger swelling than the TSA fibres and the CVI SiC matrix, with the latter two having similar swelling. The swelling mismatch between NITE SiC (~0.014) and TSA fibres (~0.009) reached up to ~0.005 at 600 °C. The higher swelling mismatch in the NITE composite increased the proportional limit after irradiation; this was interpreted as the consequence of the swelling-induced residual stresses acting to reduce the tensile thermal residual stresses that developed in the NITE process. Another work that applied Si^{2+} ion irradiation (up to 60 dpa at 300 °C) to composites with a CVI SiC matrix [19] observed a shrinkage of Hi-Nicalon^{TM} Type S (HNS) SiC fibres, with no shrinkage of TSA fibres. Shrinkage of HNS fibres was also observed under Au^{+} ion irradiation at 350 °C between 1 dpa and 50 dpa [20], leading to a significant swelling mismatch between the CVI matrix (around 0.01) and the HNS fibres (around -0.03) of up to ~0.04 at 50 dpa. In contrast to near-stoichiometric SiC fibres, such as TSA and HNS, non-stoichiometric SiC fibres exhibit substantial volume contraction with irradiation, which produces a dramatic degradation in the mechanical integrity of the composites [21,22].

These works have demonstrated the importance of swelling mismatch in the property degradation of irradiated SiC/SiC composites. The swelling mismatch interacts with the thermal mismatch strains from the materials processing, which are also affected by the ambient temperature. Third generation near-stoichiometric SiC fibres significantly reduce, but do not necessarily eliminate, the magnitude of swelling mismatch, see e.g. [19,20]. Due to experimental difficulties, measurements of residual stresses and quantitative evaluation of the damage evolution induced by swelling mismatch have been rarely reported in the literature, though theoretical analyses have been used to predict the residual stresses due to swelling mismatch, see e.g. [18,23]. Such simplified models can give a rough estimate of residual stresses of a single-fibre system, but they cannot take into account the interactions of fibre clusters and the effect of pores, for which more sophisticated numerical models are required. A recent experimental work applied post irradiation X-ray computed tomography to study the effects of the biaxial stress condition that developed, due to dimensional changes from neutron irradiation and thermal gradients, in SiC/SiC composite tubes with different architectures, such as braided and filament wound [24]. The detailed visualisation of the defects, including transverse cracking and interfacial debonding, showed the importance of transverse strength and the effect of pore morphology. This justifies the emphasis on modelling the transverse strength in the present paper.

The present study aims to provide a framework for a better mechanistic understanding and numerical simulation of the swelling-induced degradation of mechanical properties, and also to provide some trend analyses of microstructural effects on the irradiation sensitivity of SiC/SiC composites. For this purpose, numerical tests, using a microscale model based on continuum damage mechanics, are conducted to analyse the potential effects of fibre/matrix mismatch strains on the mechanical properties of SiC/SiC composites. The present focus is on unidirectional (UD) composites. Virtual unit cells with arbitrarily distributed fibres and pores will be generated. These virtual UD composites will be subject to irradiation swelling, and then loaded by monotonic tension. Macroscopic stress-strain curves of the "irradiated" composites will be obtained from these numerical tests, which allows properties such as total swelling, transverse elastic modulus and critical transverse stress to be determined. Parametric studies will also be conducted to analyse the effects of interphase strength, fibre volume fraction, as well as porosity on the predicted swelling-induced degradation of material properties. Finally, some illustrative examples demonstrate the capability of the proposed method to simulate the effects of dimensional change in the longitudinal properties of unidirectional composites.

2. Method

2.1. Virtual microstructure generation

Periodic unit cells with randomly distributed fibres are generated using a method, implemented into MATLAB scripts, which is similar to that proposed by Chateau [25]. In this method, the centres of the fibres are first randomly placed within a unit cell Ω, with each centre assigned a diameter. These diameters are randomly selected from a Gaussian distribution centred at $\bar{\phi} = 14\ \mu$m with standard deviation of 1 μm. Then, the positions of the fibre centres are iteratively adjusted by a "relaxation-vibration" technique [25], until no fibre overlapping occurs. From these fibre centres, an image of the fibres with pixel size of 0.2 μm is generated, in which the matrix is then digitally "deposited" onto fibres by image dilation from the fibre pixels. This dilation is incremental with a disk structural element of 1 pixel radius, so that it can be stopped approximately at the desired volume fraction of matrix. This digital deposition process is an analogue of the CVI matrix growth process, in which the morphology of the pores is indirectly determined by the arrangement of the fibres. The periodicity of the unit cell is taken into account during both the fibre generation and matrix generation processes. The consideration of interphase will be presented in the next section together with the discretisation of the unit cells.

Four groups of unit cells have been generated for the present study. They differ by their volume fractions of fibres: $v_f = 10\%$, $v_f = 30\%$, $v_f = 50\%$ and $v_f = 64\%$, as shown in Fig. 1. Each group contains five different unit cells with random arrangements of fibres. The dimensions have been kept as 100 μm × 100 μm for all unit cells. For the four groups of unit cells, the pore volume fractions are $v_p = 4\% \pm 0.2\%$. In order to study the porosity effect, two additional groups with two different porosities: $v_p = 10\%$ and $v_p = 15\%$ have been generated for $v_f = 30\%$ and $v_f = 64\%$.

2.2. FFT based model for multi-phase fracture

A numerical model using Fast Fourier Transform (FFT) has been recently proposed, which is able to simulate complex fracture behaviours, such as crack branching, coalescence and the competition between interfacial fracture and matrix cracking [26]. The fracture of fibres and matrix is modelled with a variational phase-field (PF) approach [27], while the interfacial behaviour (fracture and frictional sliding) is predicted by a cohesive zone (CZ) model [28]. To solve the model, an FFT solver is used [29]. This FFT based PF-CZ model is able to predict the progressive growth of both interfacial failure and matrix cracks, as well as their competition. Examples of its application can be found in [26]. The PF-CZ model involves a

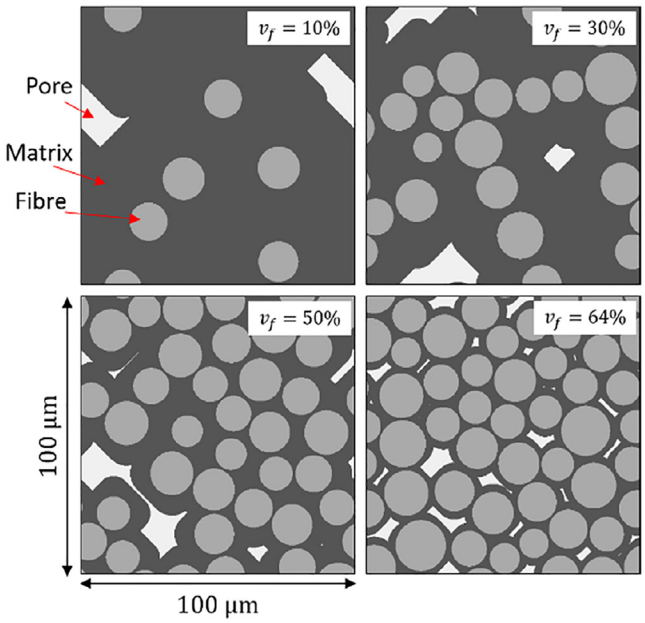

Fig. 1. Example of the virtual periodic unit cells, with different volume fractions of fibres v_f. The pore volume fractions are similar for the four unit cells ($v_p = 4\% \pm 0.2\%$).

staggered scheme, which alternately solves the mechanical equilibrium equation (with a given damage state) and the damage evolution equation (with a given stress-strain state) at each incremental time step to account for stress relaxation where damage affects the compliance.

In the FFT based method, the discretisation of unit cells needs to be structured and uniform, i.e. image-type discretisation. This significantly facilitates the model preparation step, as the digital images can be directly input into the model with no need of mesh generation in the sense of conventional finite element methods. Also, periodic boundary conditions are intrinsically prescribed in this method through the Fourier transform. Together with the periodic microstructure as presented previously, these boundary conditions produce an ideal configuration for representative volume element (RVE) analysis [30]. One drawback of image-type discretisation is that the curved surface, such as fibre-matrix interface, cannot be captured exactly. To alleviate this issue, a so-called composite voxel technique has been proposed by performing local homogenisation calculations at the interface voxels [31,32]. In our model, we have extended this technique by embedding the interphase in a set of three-layer composite voxels, whose local equilibrium and continuity conditions are governed by a laminate model, see [26] for a detailed description.

Two parameters are required in the phase-field model to describe the fracture properties: fracture toughness G_c and characteristic length l_c. These parameters approximate the strength σ_c according to $\sigma_c = \sqrt{27EG_c/256l_c}$ [33]. The cohesive zone model that simulates interphase failure uses a bilinear traction-separation law (involving a penalty stiffness $K_{I/II}$) for both mode I and mode II fractures. Two pairs of parameters characterise the fracture behaviour: fracture toughness G_{cI}, G_{cII} and strength σ_{cI}, σ_{cII}, with the subscript $*_I$ and $*_{II}$ denoting the quantities for mode I or mode II fracture, respectively. The values of the model parameters will be discussed later in Section 2.3 based on literature review.

This model has been implemented over the platform AMITEX[1] for massive parallelisation, which allows a large number of computations to be completed within a reasonable time period. Note that the model implementation is in 3D, hence the unit cells used for the study of transverse properties of UD composites have a thickness of 1 voxel in the third dimension.

[1] http://www.maisondelasimulation.fr/projects/amitex/general/_build/html/index.html#.

2.3. Irradiation effects: swelling, elastic and fracture properties

2.3.1. Swelling

Irradiation swelling can cause property degradation of SiC/SiC composites, see, e.g. [1,23,34,35]. At a given irradiation temperature, the swelling of SiC/SiC composites as well as of the CVI SiC matrix exhibits a dose-independent plateau for a large range of irradiation doses (approximately 1 ~ 70 dpa) [21,36], whereas the magnitude of swelling decreases with increasing irradiation temperature in the range of 150 °C – 1000 °C. To represent this, and to place the results in the context of likely operating conditions for easier interpretation, three irradiation temperatures are investigated in the present work: 300 °C, 500 °C and 800 °C, to be representative of the potential temperatures in various advanced reactors. Due to the plateau, the dose effect is excluded, i.e. swelling data representing the dose-insensitive range will be used. Representative swellings of the SiC matrix (s_m) at different irradiation temperatures are taken from experimental measurements found in the literature [21]: $s_m = 0.02$, $s_m = 0.01$ and $s_m = 0.007$ for 300 °C, 500 °C and 800 °C, respectively. Very limited data have been reported for swelling of SiC fibres. Therefore, to investigate the sensitivity to this, we use various assumed fibre swellings, which are calculated relative to the matrix swelling at each irradiation temperature: $s_f = (1+\gamma)s_m$, with γ varying from -0.5 to 0.5 for 300 °C and 800 °C, and from -1.5 to 1.5 for 500 °C. The range of values of γ at 500 °C was wider in order to achieve larger swelling mismatches, which promote more significant effects on the mechanical properties of the composites. This helps to extend the parameter space of the present investigation.

2.3.2. Elastic constants

The elastic modulus of the SiC matrix has been shown to change with irradiation temperature [3]. Katoh et al. [37] identified a linear dependence of the elastic modulus versus the swelling of CVI SiC. According to the data provided by [37], we identify the linear expression as $E_m = E_{m0}(1 - 3.3s_m)$, where the initial elastic modulus $E_{m0} = 440\ 440$ GPa and s_m the swelling of matrix. This leads to $E_m = 411\ 411$ GPa, $E_m = 425\ 425$ GPa and $E_m = 430\ 430$ GPa for 300 °C, 500 °C and 800 °C, respectively. Note that these changes of elastic modulus are small and will lead to an insignificant effect on the macroscopic properties of the composites (see later in Section 3.1). The Poisson's ratio of CVI SiC has been reported within a range of 0.1~0.2, with negligible temperature dependency. In the present study, we follow the Handbook of [3] taking the value of $\nu_m = 0.2$ as the Poisson's ratio for all temperatures under investigation. Noting the weak effect of irradiation on the elastic properties of the SiC matrix, the irradiation effect on the elastic properties of SiC fibres is neglected. The modulus $E_f = 365\ 365$ MPa and Poisson's ratio $\nu_f = 0.2$ measured at unirradiated condition [38] are taken for all simulations.

2.3.3. Fracture properties

The strength of the SiC matrix has been measured in the literature, but shows a large range due to differences in size and geometry of specimens tested by different methods, as these can affect the characteristic length of defects. For example, using a microtesting method, Zayachuk et al. [38] recently reported a strength of 21.5 GPa, which is much higher than classical macroscopic tests (such as 4-point bend, O-ring compression, internal pressurization) for which a wide range between 0.2 GPa and 3 GPa is reported [3]. In the present work, the tensile strength of the SiC

matrix is assumed to be approximately 1 GPa, corresponding to a characteristic length of 0.002 mm for the chosen value of G_c. This is obtained through the relation $G_c = K_{Ic}^2/E$, where the fracture toughness G_c is estimated from the critical stress intensity factor K_{Ic} (4.25 MPa·m$^{1/2}$) measured by Zayachuk et al. [38], leading to $G_c = 0.04$ N/mm. When considering transverse loads, fibre fracture is assumed not to occur. Therefore, a nominal high fracture toughness is assigned to fibres with $G_c^{fibre} = 100$ N/mm. The characteristic length is also taken as $l_c^{fibre} = 0.002\ 002$ mm due to the structural similarity between fibres and matrix. In order to investigate the significance of swelling mismatch, the fracture properties of the fibres and matrix are assumed to be unaffected by irradiation, as justified by the work of Price [39,40].

In the cohesive zone model for the PyC interphase, mode I and mode II are assumed to have the same fracture strength and toughness. We take the critical stress as $\sigma_{cI} = \sigma_{cII} = 300$ MPa [41]. As for the fracture energy, the approximate value is calculated using $G_{cI/cII} = K_{Ic}^2/E$, together with the measurement of $K_{Ic} = 0.8\ 8$ MPa m$^{1/2}$ from [38] and the assumption of $E = 30$ GPa for the elastic modulus of the interphase. This leads to $G_{cI} = G_{cII} = 0.02$ N/mm. The shape ratio η is set to 0.999, resulting in a penalty stiffness of $K_I = K_{II} = 2 \times 10^9$ N/mm^3, such that the elastic deformation of the interphase is small compared to those of the neighbouring fibre and matrix. The friction coefficient is taken as $\mu^I = 0.25$ [41]. Although a decrease in interphase shear strength due to irradiation was observed by Nozawa et al. [16,41], the fact that the interphase initially is much weaker than both fibres and matrix will make this irradiation effect negligible comparing to the property changes of the two other constituents. Therefore, we maintain the same interphase properties for all irradiation conditions. In addition, the case of a strong interphase with $\sigma_{cI} = \sigma_{cII} = 3000\ 3000$ MPa will be studied to provide a comparison.

Note that due to the current lack of reliable experimental data, the parameters of the fracture properties chosen herein are an approximation. The aim of this work is to provide a framework that could examine the sensitivity to these parameters, and thus to guide their future measurements.

2.4. Numerical virtual tests

Numerical simulations of the virtually generated unit cells have been conducted for different swelling mismatches at three different irradiation temperatures. In the present model, the irradiation induced degradation on elastic modulus of matrix and the swellings of matrix and fibres at different temperatures are implemented via a lookup table (Section 2.3). Each unit cell is subject to two steps of loading:

Step 1 – Swelling The swelling of fibres and matrix are taken into account in the model by applying an expansion strain $\boldsymbol{\varepsilon}_f$ to fibres and $\boldsymbol{\varepsilon}_m$ to matrix, before any external mechanical loads are applied (the unit cell is free of external stresses, and has no internal stresses prior to the irradiation). The expansion strains are calculated by the volumetric swelling of fibres (s_f) or matrix (s_m): $\boldsymbol{\varepsilon}_{f/m} = \frac{1}{3} s_{f/m} \mathbf{I}$, with $\mathbf{I}$ the 3 × 3 identity matrix. Interphase swelling is neglected in this study, due to its very small thickness (~100 nm) and its relatively high compliance compared to SiC [42]. After this process, internal residual stresses, as well as local damage (interphase fracture or matrix cracking), may be produced due to the swelling mismatch between fibres and matrix.

Step 2 – Tension To determine the mechanical properties of such an "irradiated" composite, a monotonic tension is then applied to the unit cell either in the transverse (i.e. perpendicular to the fibres) or the longitudinal (parallel to the fibres) direction. From this virtual test a stress-strain curve is produced, with an example for transverse loading shown in Fig. 2.

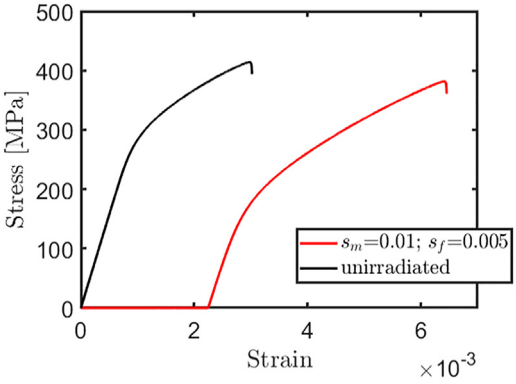

Fig. 2. Example of typical stress-strain curves of numerical virtual tests for transverse loading of a unit cell with $v_f = 64\%$, $v_p = 4\%$ and weak interphase: black curve – unirradiated composite (no swelling), red curve – irradiated composite with matrix swelling of $s_m = 0.01$ and fibre swelling of $s_f = 0.005$.

The simulations allow us to determine the total swelling, the elastic modulus and the critical tensile stress at peak load (strength) of the composite. The predicted stress-strain curve for the unirradiated condition of the same composite will be used as reference to quantify the degradation of modulus and strength.

In order to take into account the variations of interphase strength, swelling mismatch, fibre volume fraction and porosity, a total number of 810 simulations have been conducted in the present work. Each simulation involved a unit cell of 250,000 discretisation voxels plus a number of composite voxels (depending on the fibre volume fraction), which produce even more degrees of freedom. This large amount of computations were performed over the Advanced Research Computing (ARC) system of Oxford University. Each single simulation was parallelised on one compute node with 16 processors taking 1~3 h.

3. Results and discussions

The present objective of this work is to provide some trend analyses of swelling mismatch effects on mechanical properties, rather than to accurately predict their values. For the latter purpose, more reliable measurements on the constituents' properties will be required, which are not yet available. Results for the unit cells with 64% fibres and 4% pores will be first presented to illustrate the effects of swelling mismatch on various properties of the composites. Then, results from the unit cells with different fibre densities and porosities will be presented to illustrate the effects of these two microstructural parameters. It should be noted that the CVI process does not typically achieve an overall porosity as low as 4%, but this may be achievable at local scales. Furthermore, a similar trend in the sensitivity to swelling mismatch is observed for higher porosities (see Section 3.3), which suggests that the observation from this 4% porosity example should also be valid for higher porosities (up to 15%).

We recall that the focus of the present work is on the transverse properties of UD composites, and some illustrative results on longitudinal behaviour will be shown in Section 3.5. Together, these are relevant to possible effects of hoop, axial and radial stresses in filament wound or braided composites. The model has been implemented in 3D, therefore, the unit cells used for the study of transverse properties (Sections 3.1–3.4) have 1 voxel thickness in the third direction.

3.1. Comparison between strong and weak interphases

This section compares the swelling effects of composites with weak or strong interphases to investigate the effect of interphase

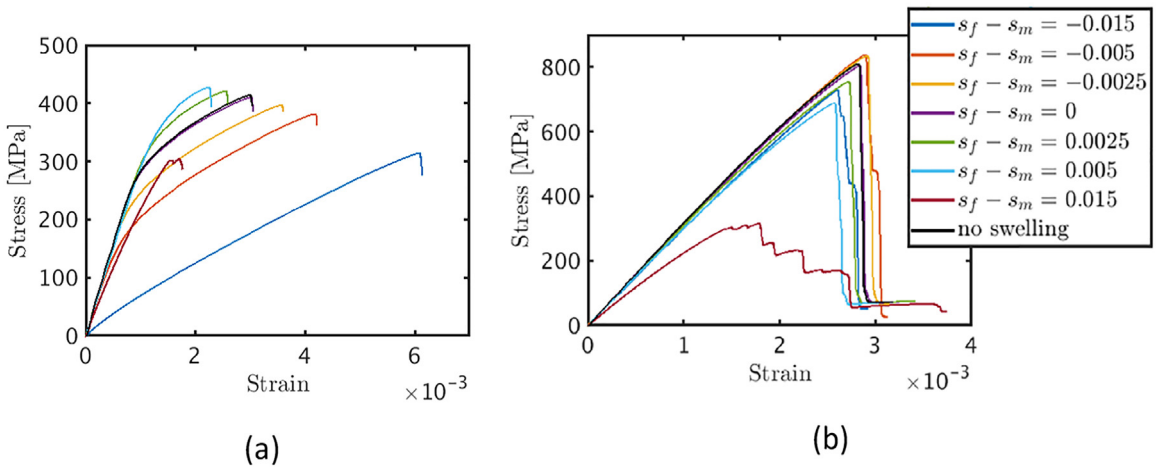

Fig. 3. Stress-strain curves for transverse loading of a UD composite with $v_f = 64\%$ and $v_p = 4\%$ irradiated at 500 °C ($s_m = 0.01$), with (a) weak interphase, (b) strong interphase. All curves have been shifted to the origin by subtracting a strain offset, which is the swelling-induced strain of the composite. The stress-strain curve for the unirradiated condition (no swelling) is shown in black as a reference.

strength. The study does not aim to predict the mechanical behaviour of a particular SiC/SiC composite under a given irradiation condition, so the strong interface analysed in this work serves as a comparison to the weak-interphase composites to illustrate the potential range of behaviour. Nonetheless, the results for the strong interphase may be relevant for other CMCs, such as C/C or oxide/oxide, whose fibre-matrix interface is strong. Significant residual stresses in such systems may be induced by the mismatch of coefficient of thermal expansion (CTE) between fibres and matrix [43], with damage developing on cooling from high temperature processing in a manner that is quite similar to the present analyses.

3.1.1. Stress-strain curves

Fig. 3 shows example stress-strain curves for different fibre swellings of a unit cell with $v_f = 64\%$ irradiated at 500 °C ($s_m = 0.01$). The unirradiated composite (no swelling) is included to provide a reference. The unirradiated weak-interphase composite exhibits obvious nonlinearity before failure, while the strong-interphase composite shows linear behaviour. As will be seen later in Section 3.1.2, nonlinearity is the macroscopic consequence of fibre-matrix debonding, which occurs for the weak interphase and not the strong interphase. Such nonlinearity is also observed at moderate swelling mismatch ($-0.005 \leq s_f - s_m \leq 0.005$), and the corresponding proportional limit decreases for negative mismatch and increases for positive mismatch. At large negative mismatch ($s_f - s_m = -0.015$), the weak-interphase composite exhibits a quasi-linear curve with a much lower initial elastic slope; significant debonding between fibres and matrix makes the composite approximate to a porous SiC matrix. The same large negative swelling mismatch leads to no significant effect for the strong-interphase composite. For the case of $s_f - s_m = 0.015$, the stress-strain curves show a clear decrease in elastic modulus and peak load for both weak and strong interphases. This distinct behaviour should be related to the significant matrix damage (see later in Section 3.1.2) created by the large positive swelling mismatch. The strong interface composite exhibits a larger post-peak strain, which is a consequence of the clamping stress between fibres and matrix. For both weak and strong interphases, the irradiated stress-strain curve with no swelling mismatch ($s_f = s_m$) appears identical to the unirradiated condition (superimposed curves). This shows that the slight irradiation-induced decrease in the elastic modulus of SiC matrix produces a negligible effect on the macroscopic properties of the composites, as mentioned in Section 2.3.2.

3.1.2. Internal residual stresses and damage

Maps of internal residual stresses (expressed as maximum principal stress σ_{max}) and the damage induced by different irradiation swelling mismatches before the application of the mechanical load are shown in Fig. 4 for both weak and strong interphases. Overall, the matrix is mostly under compression at negative swelling mismatch ($s_f < s_m$), and tension at positive mismatch ($s_f > s_m$). The residual stresses are similar for the weak and strong interphases at positive mismatch, and also for low-magnitude negative mismatch (e.g. $s_f - s_m = -0.005$). However, when the fibres swell significantly less than the matrix ($s_f - s_m = -0.015$), the weak-interphase composite has lower-magnitude residual stresses than the strong-interphase composite. This results from fibre-matrix debonding, which occurs for the weak interphases and not for strong interphases, as shown in Fig. 4.b. The significant interphase fracture at $s_f - s_m = -0.015$ also explains the significant degradation in initial elastic modulus observed in Fig. 3.a.

Histograms of residual stresses (measured in each pixel) at different swelling mismatches are gathered in Fig. 5, supporting the observations of Fig. 4. Each mismatch produces a bi-modal distribution of stresses, showing peaks that correspond to stresses in either fibres or matrix. The distribution of stresses is almost identical for weak-interphase and strong-interphase composites with positive mismatch (curves in purple and blue) and low-magnitude negative mismatch (curves in green). For high-magnitude negative mismatch (curves in red), the weak-interphase composite exhibits a lower mode value of the fibre stresses than the strong-interphase composite, which is the consequence of fibre-matrix debonding. Note that the calculation of the maximum principal stresses takes into account the positive and negative signs of the eigenstresses, which makes it irrelevant to analyse the compressive-stress peaks of the histograms. Therefore, only the tensile-stress peaks (fibre-mode for negative mismatch and matrix-mode for positive mismatch) will be used to analyse the stress distributions in the following.

3.1.3. Effects of irradiation swelling on overall properties

From the simulated stress-strain curves, three overall characteristics of each tested composite are extracted: total swelling, initial transverse elastic modulus and transverse strength.

3.1.3.1. Total swelling. The total swelling of an irradiated composite is evaluated in the numerical simulations as the trace of the predicted overall strain tensor $s^{sim} = \bar{\varepsilon}_{xx} + \bar{\varepsilon}_{yy} + \bar{\varepsilon}_{zz}$. Alternatively, we

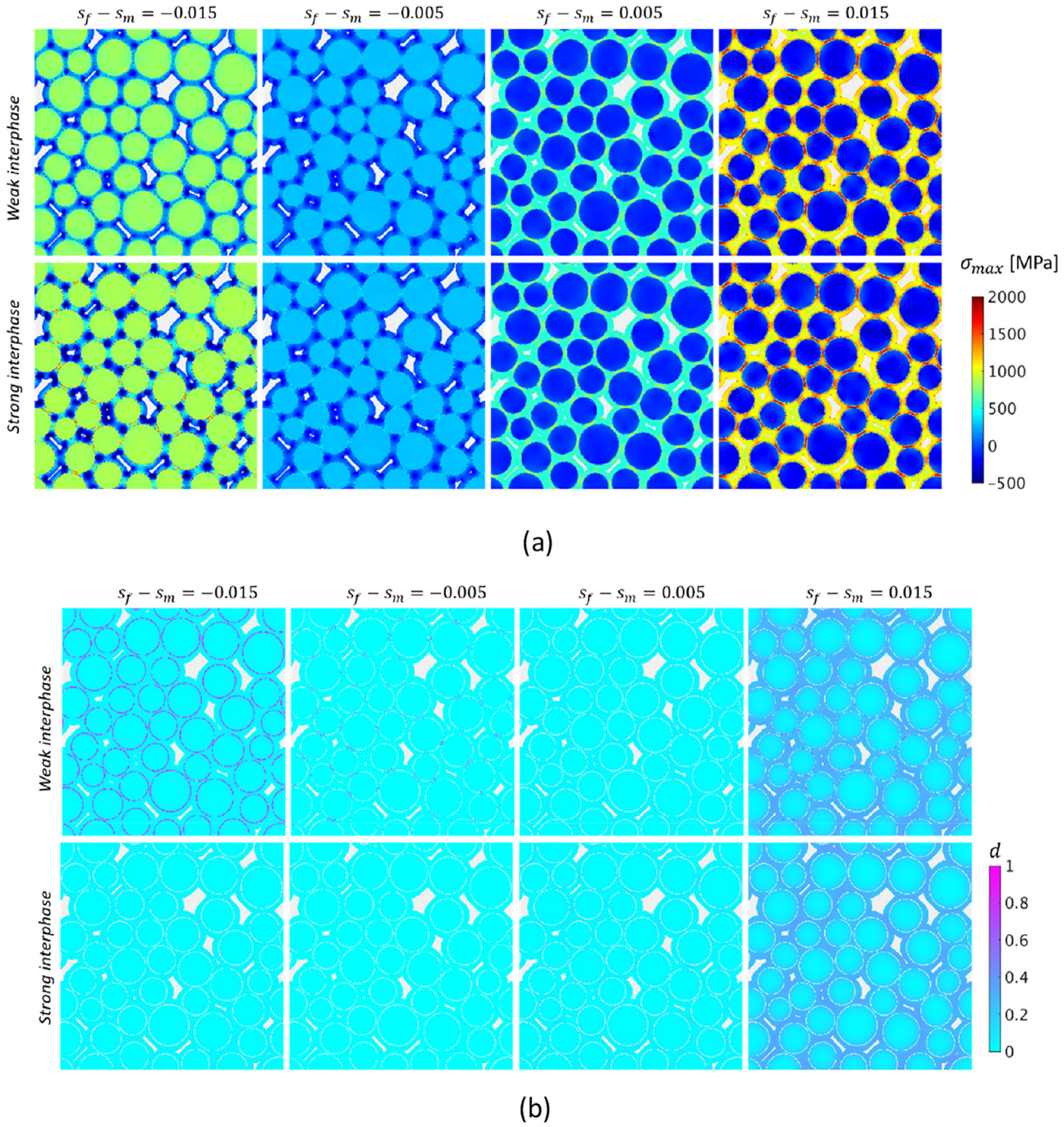

Fig. 4. Maps of (a) residual stresses and (b) damage induced by different swelling mismatches for a unit cell with weak or strong interphase. The volume fractions of fibres and pores are 64% and 4%, respectively.

can use a simple volume average to approximate the total swelling as

$$s^{theor} = \frac{v_f s_f + v_m s_m}{v_f + v_m} \tag{1}$$

where v_f and v_m are the volume fractions of fibres and matrix in the composite, respectively. The values calculated from this formula will be referred to as theoretical values. Note that the underlying assumption for Eq. (1) is that no kinematic discontinuity occurs in the composite.

A comparison between the total swelling determined from the numerical simulations and that from the simple theoretical formula is shown in Fig. 6. We recall that each data point corresponds to five independent simulations with similar yet different unit cells, and the error bar is the standard deviation of the five results. Overall, the data for the different irradiation temperatures follow the same trend curve. This is consistent with the negligible effect of the change in elastic modulus of the SiC matrix (as this is the only difference related to irradiation temperature in the present model). For the weak-interphase composites, both negative ($s_f < s_m$) and positive ($s_f > s_m$) swelling mismatch with high absolute values produce total swellings of the composites that are larger than the theoretical values; whereas, for the strong-interphase composites, the over-swelling induced by negative mismatch is dramatically reduced. The negative mismatch with high absolute values induces strong tensile stresses at

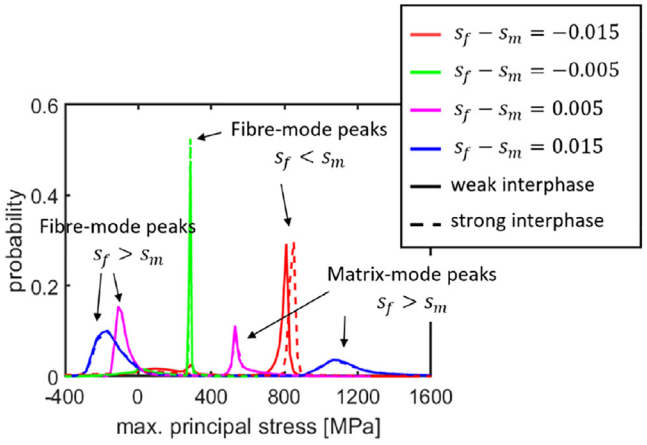

Fig. 5. Histograms of maximum principal stresses of a composite with $v_f = 64\%$ and $v_p = 4\%$ under different swelling mismatches. The results for weak interphase and strong interphase are compared in the same graph. Bimodal peaks are indicated by the arrows, except the matrix-mode peaks for $s_f < s_m$ that are much lower than the corresponding fibre-mode peaks.

fibre-matrix interphase (Fig. 4.a left column), so debonding occurs if the interphase is weak (Fig. 4.b left column), producing over-swelling of the composite. On the other hand, fibres that swell much more than the matrix produce high tensile stresses in the matrix (Fig. 4.a right column), while the interphase is under compression. Therefore, for both weak and strong interphases, matrix damage is responsible for the over-swelling of the composite at positive swelling mismatch (Fig. 4.b right column).

The total swellings calculated for different swelling mismatches are collected in Appendix A. The results lie in the range of the literature measurements of various SiC/SiC composites made by different types of fibres, see e.g. [21,22,44]. To demonstrate how the modelling can help interpret experimental observation, we cite the work of [21], in which the neutron irradiation performance of two types of SiC/SiC composites, based on Hi-Nicalon (HN) and Hi-Nicalon type S (HNS) with the same CVI SiC matrix, is compared. At 800 °C, the HNS composites exhibited a total swelling comparable to that of the SiC matrix (~0.007); whereas the total swelling of the HN composites was smaller (~0.005). This implies that at 800 °C, the HNS fibres exhibit a similar swelling as the SiC matrix, while the HN fibres swell less than the matrix (negative mismatch). According to our simulation results, such a relatively strong negative swelling mismatch could produce dramatic interfacial debonding (e.g. Fig. 4). This is consistent with the experimental observation of reduced strength in the irradiated HN composite.

3.1.3.2. Transverse elastic modulus. To show the effect of swelling mismatch on the degradation in transverse elastic modulus of the composites, we normalise the measurements by the elastic modulus of the unirradiated composite (referred to as *unirradiated modulus*). Under the unirradiated condition, the moduli for the weak-interphase and strong-interphase composites are similar, i.e. 297 (±18) GPa versus 304 (±18) GPa. The results for all irradiation temperatures and different swelling mismatches are gathered in Fig. 7. Similar to the total swelling, the measurements for the three different irradiation temperatures follow the same trend curves. No significant degradation in elastic modulus is produced at any irradiation temperature if the swelling mismatch is small or negligible between fibres and matrix. When the fibres swell more than the matrix ($s_f > s_m$), the trend is quasi-identical between weak and strong interphases, both showing an increasing degradation of elastic modulus with increasing mismatch. In contrast, quite different degradation trends are observed between the weak and strong interphases for negative mismatch ($s_f < s_m$). The weak-interphase composites (Fig. 7.a) exhibit a sharp decline (up to 75%) of elastic modulus after a certain threshold of swelling mismatch (~0.003); whereas no significant decrease is observed in the elastic modulus of the strong-interphase composites (Fig. 7.b). By inspection of the residual stresses and damage shown in Fig. 4, the modulus degradation at positive swelling mismatch is due to matrix damage, while that at negative mismatch is due to fibre-matrix debonding.

3.1.3.3. Transverse strength. Fig. 8 shows the effect of swelling mismatch on the transverse strength (i.e. critical stress) of the simulated composites. The critical stresses are normalised by the values from unirradiated condition (referred to as *unirradiated strength*). Under the unirradiated condition, the weak-interphase composites exhibit a lower strength than the strong-interphase composites, i.e. 376 (±42) MPa versus 705 (±102) MPa. Different degradation trends between weak and strong interphases are observed at both negative and positive mismatches.

At negative mismatch ($s_f < s_m$), the strength for the weak-interphase composites monotonically decreases as the magnitude of the mismatch increases; whereas the strong-interphase composites exhibit an increase of strength at low-level negative mismatch. This strengthening effect diminishes as the mismatch magnitude increases, and is accompanied by a larger variation between different fibre distributions (shown by the standard deviation). The strengthening effect is related to the fact that matrix cracking is the dominant damage mechanism in strong-interphase composites.

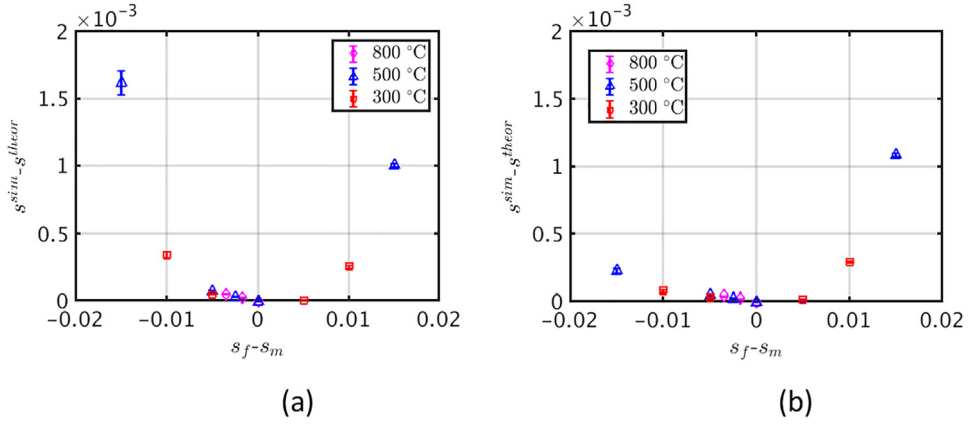

Fig. 6. Difference between the simulated total swelling and the theoretical value of composites with 64% fibres and 4% porosity for different swelling mismatches $s_f - s_m$: (a) weak interphase, (b) strong interphase. Data obtained from different irradiation temperatures are indicated by different colours.

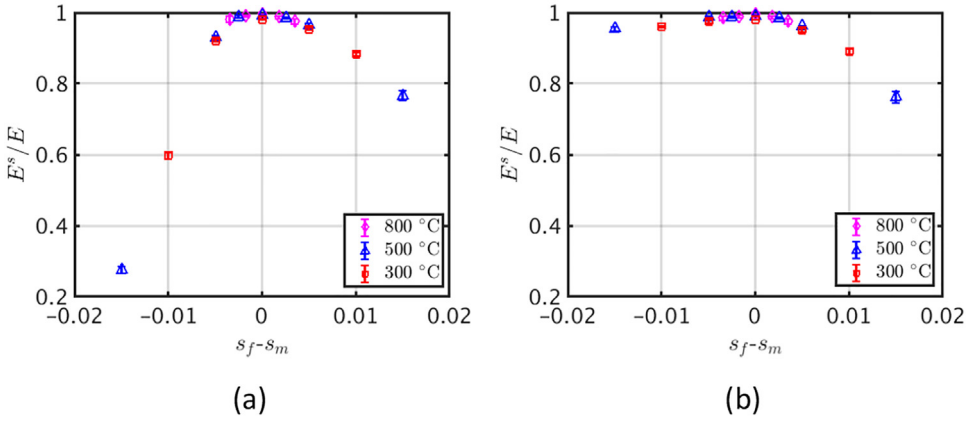

Fig. 7. Effect of swelling mismatch on the degradation of transverse elastic modulus of UD composites with 64% fibres and 4% pores: (a) weak interphase, (b) strong interphase.

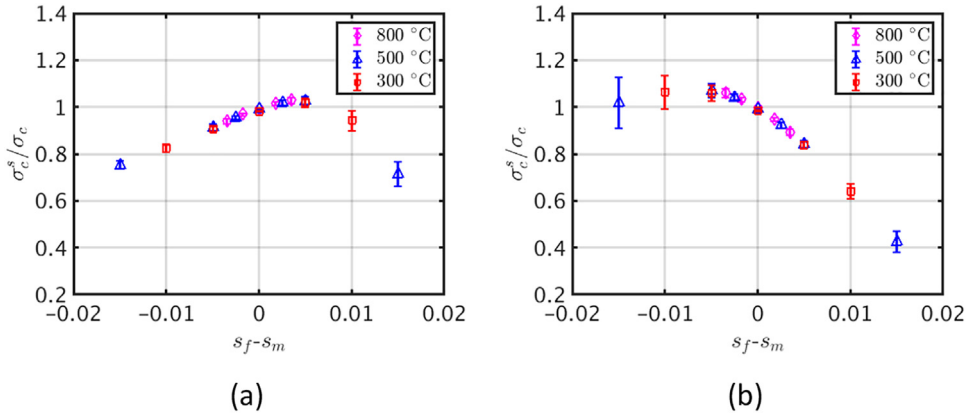

Fig. 8. Effect of swelling mismatch on the transverse strength of UD composites with 64% fibres and 4% pores: (a) weak interphase, (b) strong interphase.

At moderate negative mismatch, the matrix in strong-interphase composites is pre-stressed in compression without damaging the interphase (Fig. 4.b left column), which suppresses the propagation of matrix damage during the later transverse loading stage.

At positive mismatch ($s_f > s_m$), the strong-interphase composites exhibit a monotonously decreasing strength with increasing swelling mismatch; whereas the weak-interphase composites retain or even slightly increase their strengths at small mismatch values ($0 < s_f - s_m < 0.005$), followed by a marked decline of the critical stress for high mismatch values. The slight strengthening is due to the fact that the strength of weak-interphase composites is mainly governed by interfacial debonding, which can be suppressed to some extent due to the initial compressive state of the interphase at low-magnitude positive mismatch (Fig. 4).

3.2. Effect of fibre volume fraction (weak interphase composites)

Keeping the same porosity of $v_p = 4\%$, unit cells of different fibre volume fractions have been tested: $v_f = 10\%$, $v_f = 30\%$, $v_f = 50\%$ and $v_f = 64\%$. Only the weak interphase case that approximates the typical situation of as-manufactured SiC/SiC composites is considered in this analysis. Following the effect of fibre volume fraction on the unirradiated modulus and strength, the sensitivity of different fibre volume fractions to irradiation swelling will be analysed.

3.2.1. Unirradiated properties

The unirradiated transverse modulus and strength as functions of fibre volume fractions are plotted in Fig. 9. Both properties

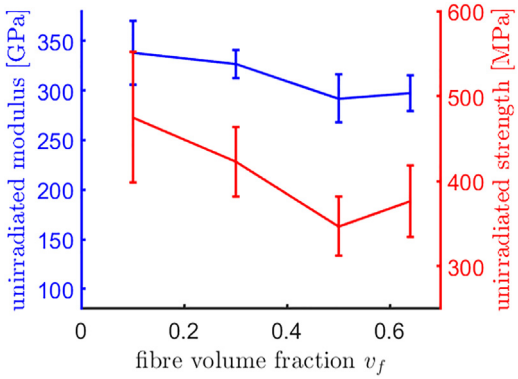

Fig. 9. Transverse elastic modulus and strength of unirradiated UD composites with the same porosity ($v_p = 4\%$) and various fibre volume fractions. The error bars are the standard deviations of the measurements from five different unit cells with a same fibre volume fraction.

exhibit a decrease from $v_f = 10\%$ to $v_f = 50\%$ and then a slight increase at $v_f = 64\%$. The drop in modulus and strength up to $v_f \leq 50\%$ is due to the smaller modulus of fibres and the lower strength of the weak interphase. For the same fibre volume fraction, a large variation (shown by the standard deviation) is observed at each measurement point. This suggests that the arrangement of fibres has an important effect on the transverse elastic modulus and transverse strength of these composites.

In order to test whether the relative position of the fibre-matrix interphases induces a significant effect, we performed five simu-

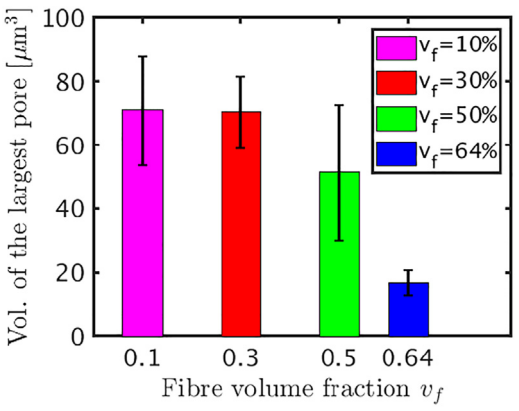

Fig. 10. Volume of the largest pore in each unit cell with the same porosity (v_p = 4%) and different fibre volume fractions. The error bars indicate the standard deviations of the measurements from five different unit cells with a same fibre volume fraction.

lations using unit cells with no pores, yet having the same fibre volume fraction ($v_f = 30\%$). The predicted average modulus and strength are 407 GPa and 635 MPa with standard deviations of 0 GPa and 36 MPa, respectively. This shows that the fibre clustering alone has an effect on the strength but no effect on the elastic modulus of the composites.

Therefore, the variation in elastic modulus shown in Fig. 9 is deduced to be caused by the differences in the pore morphology. The arrangement of fibres not only determines the relative positions of fibre-matrix interphases that can be considered as weak points in the SiC/SiC composites, it also affects the morphology of the pores. Pore shape and orientation are well known to affect significantly the elastic modulus and strength of porous media [45–47].

The effect of fibre volume fraction on pore size is shown in Fig. 10. For $v_f \leq 50\%$, the size of the largest pore exhibits a relatively great variation and decreases slightly with increasing fibre volume fraction. A marked decline of the largest pore size with a smaller variation is observed at $v_f = 64\%$, indicating that the high fibre volume fraction (64%) gives a more uniform distribution of the constituents. This makes it difficult to form fibre clusters that promote larger pores, thus restricting the formation of damage localisation under the transverse load. This could be an underlying cause of the slight increase of modulus and strength for $v_f = 64\%$ observed in Fig. 9.

3.2.2. Sensitivity to irradiation swelling

The property changes induced by swelling mismatch are shown in Fig. 11 for different fibre volume fractions. Overall, the macroscopic quantities (total swelling, transverse elastic modulus and strength) exhibit increasing sensitivity to irradiation swelling as the fibre volume fraction increases until $v_f \leq 50\%$. The highest fibre volume fraction ($v_f = 64\%$) produces a sensitivity that is either lower than or comparable to the fibre volume fraction of 50%. Two particular points are noted below.

First, the transverse modulus degradation at negative mismatch shows a sharp drop at around $s_f - s_m = -0.005$. For mismatch smaller than -0.005, the rate of change of modulus degradation with mismatch becomes smaller, and the degradation even becomes insensitive to the mismatch magnitude for the lowest fibre volume fraction ($v_f = 10\%$). This critical swelling mismatch (-0.005) corresponds to the situation where the interface critical stress is reached, creating significant interfacial debonding. However, such a strong sensitivity does not appear for the strength, because the transverse strength of the composites at negative mismatch is more sensitive to matrix damage than interfacial debonding.

Second, the modulus and strength and their variabilities at positive mismatch for the moderate fibre volume fractions (30% and 50%) are more sensitive to swelling mismatch than for the lowest and highest fibre volume fractions (10% and 64%). This will be discussed in the following section together with the distributions of residual stresses and damage.

3.2.3. Residual stresses and damage

Some typical stress maps for the four different fibre volume fractions are given in Fig. 12 at different swelling mismatches. Overall, a negative mismatch induces tension in fibres and compression in matrix, and vice-versa for a positive mismatch. Due to the geometric differences of the two constituents, the high tensile stresses in fibres at negative mismatch are confined within the individual fibres, while the stress concentrations in the matrix at positive mismatch may form a larger network connecting adjacent weak points – the interphases. This latter effect appears more pronounced in the composites with lower fibre volume fractions (10% and 30%). These networks of matrix damage demonstrate the importance of fibre clustering to the transverse properties and their variabilities at positive mismatch (Fig. 11.b and c).

SiC matrix is a ceramic with brittle failure properties, therefore, its fracture is mainly governed by the local maximum principal stress and the weakest-link probability. This means that the composite fails only when the amount of “hot spots” (i.e. where the stress is higher than the critical value for SiC matrix) become substantial under external load. In the case of $v_f = 10\%$, although stress concentrations occur, their effect is small due to the small number of fibres. In the case of $v_f = 64\%$, stress is relatively uniformly distributed, which also reduces the amount of “hot spots” during the damage propagation due to external load. Therefore, the absolute values of transverse properties are less sensitive to irradiation swelling mismatch for the lowest and the highest fibre volume fractions, as observed in Fig. 11. Both stress concentration and average stress magnitude affect the composite’s failure. More detailed investigations are needed to judge which factor prevails for different fibre volume fractions.

The same argument also explains the variabilities of transverse properties. Fibre clustering has random characteristics, leading to variability in matrix damage networks. This variability is barely manifested in the macroscopic properties of the composites with the lowest fibre volume fraction (10%) where the fibre clusters are more isolated. On the other hand, the highest fibre volume fraction (64%) leads to the fibres being more uniformly distributed with a smaller inter-fibre separation. Therefore, both the lowest and the highest fibre volume fractions exhibit lower variability in the degradation of transverse modulus and strength in response to irradiation swelling.

Histograms of the residual stresses in fibres or matrix for composites with different fibre volume fractions are plotted in Fig. 13. It has been checked that (not shown here) the unit cells with a same fibre volume fraction all produce very similar histograms to each other including the positions and shapes of the peaks. For negative mismatch (Fig. 13.a), the peak stress (fibre-mode peaks) moves towards smaller mode value with increasing fibre volume fraction. This is mainly related to the change in compliance of the surrounding composite medium (matrix, fibres and interphases) of each fibre, i.e. the surrounding compliance is greater for a higher fibre volume fraction, as the fibre modulus is lower than that of the matrix. In contrast, the matrix-mode peak for positive mismatch (Fig. 13.b) moves towards larger mode values as the fibre volume fraction increases, due to the decreasing volume of the continuous matrix that accommodates the strains induced by the relative swelling of the fibres. Furthermore, the higher-value tails

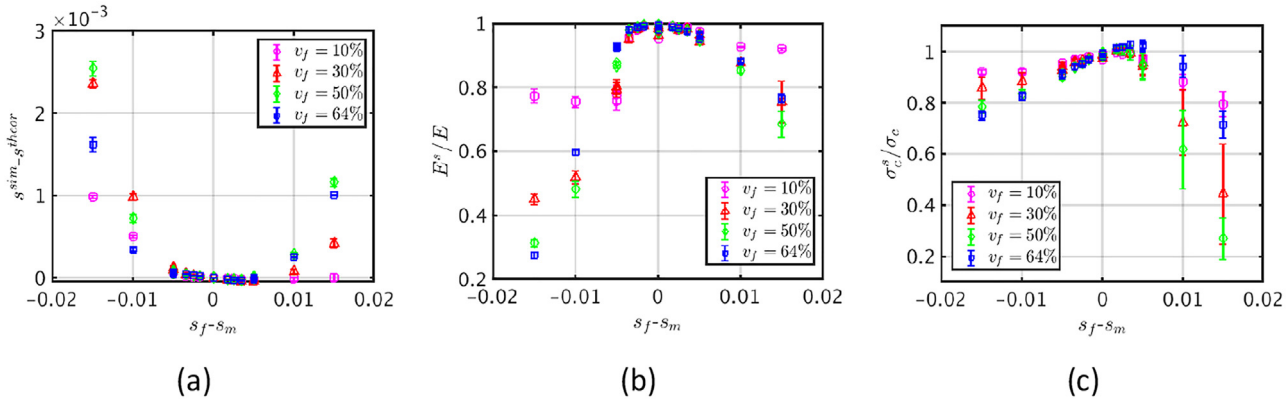

Fig. 11. Property changes induced by swelling mismatch in weak-interphase composites with the same porosity ($v_p = 4\%$) and different fibre volume fractions: (a) over-swelling, (b) degradation in transverse elastic modulus, (c) degradation in transverse strength.

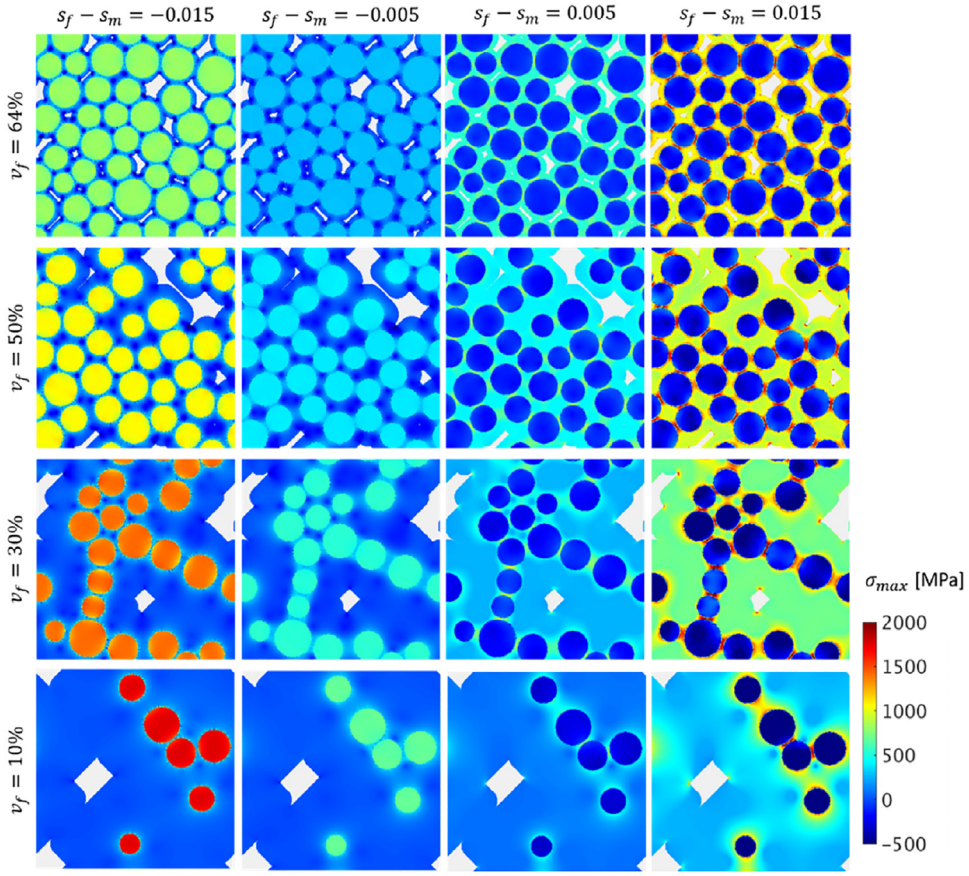

Fig. 12. Residual stresses induced by different swelling mismatches for unit cells with the same porosity ($v_p = 4\%$) and different fibre volume fractions.

of the peaks for negative mismatch seem to be cut off, which can be attributed to the partial fibre-matrix debonding that relaxes the stresses in the fibres. In contrast, long high-value tails of the peaks are observed for positive mismatch, which are consistent with the strongly heterogeneous distributions of stresses shown in Fig. 12.

In order to examine the overall damage of the composites at this initial unloaded stage, we define two damage parameters $\bar{D}_{int} = \frac{1}{\Omega_{int}} \int_{\Omega_{int}} d(\underline{x}) d\underline{x}$ and $\bar{D}_{mat} = \frac{1}{\Omega_{mat}} \int_{\Omega_{mat}} d(\underline{x}) d\underline{x}$, where Ω_{int} and Ω_{mat} are the regions of interphase and the matrix, respectively. These two parameters are used to quantify the damage level of interfacial debonding at negative mismatch and the matrix damage at positive mismatch, respectively. Their values are plotted in Fig. 14 as functions of fibre volume fractions. For negative mismatch (Fig. 14.a), the interfacial damage becomes less severe when the fibre volume fraction increases, though it remains high at the high-magnitude negative mismatch ($s_f - s_m = -0.015$). The decrease in interfacial damage is consistent with the decreasing stresses in fibres at negative mismatch (Fig. 13.a). In contrast, for positive mismatch (Fig. 14.b), increasing the fibre volume fraction induces more severe matrix damage, which is consistent with the increasing matrix stress observed in Fig. 13.b. Interestingly, the rate of increase of the overall matrix damage is smaller from $v_f = 50\%$ to $v_f = 64\%$. This may be related to the relatively uniform distribution of constituents in the composites with high fibre volume fraction (64%). A summary of the damage fields for four different fibre volume fractions are given in Appendix B.

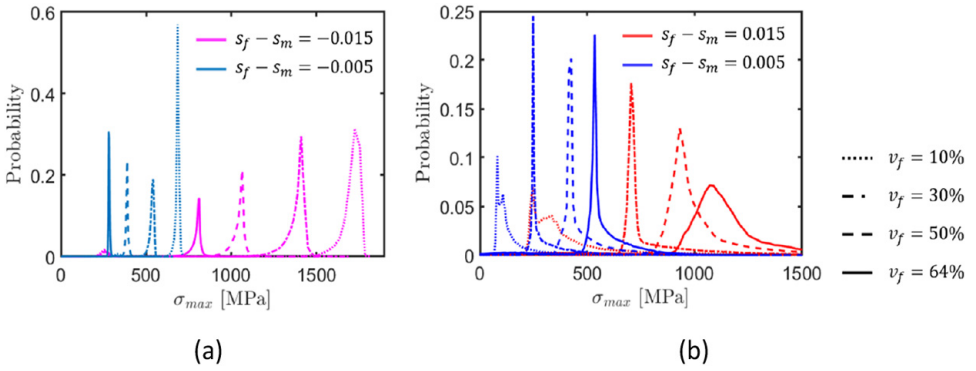

Fig. 13. Histograms of the maximum principal stresses in (a) fibres and (b) matrix of unit cells with weak interphase, $v_p = 4\%$ and different fibre contents: (a) showing the statistics in the fibres of the composites under negative mismatch, $s_f < s_m$; (b) showing the statistics in the matrix of the composites under positive mismatch, $s_f > s_m$.

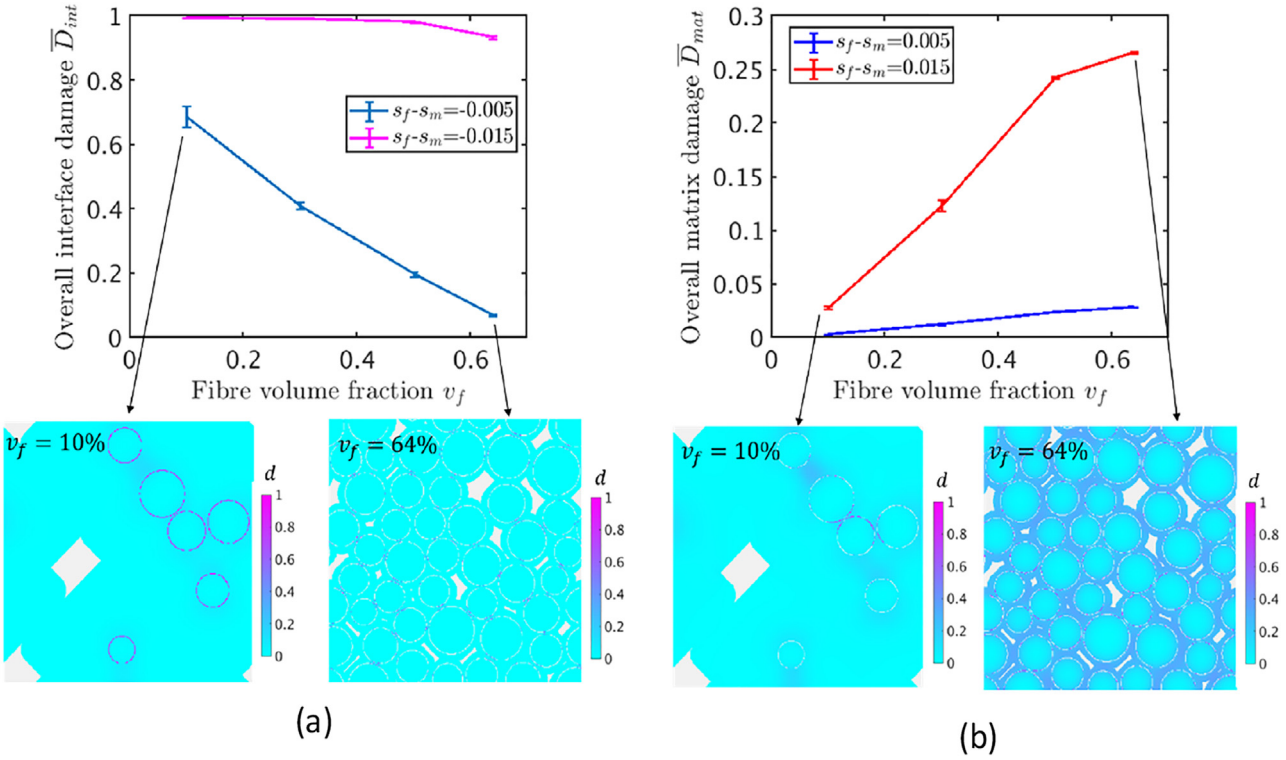

Fig. 14. Overall damage induced by swelling mismatch for unit cells with the same porosity ($v_p = 4\%$) and different fibre volume fractions: (a) for interfacial damage at negative mismatch; (b) for matrix damage at positive mismatch. Examples of the damage fields are also given for the lowest and the highest fibre volume fractions at specific mismatch.

In the case of positive swelling mismatch, the residual stresses (Fig. 13.b) and the initial damage density (Fig. 14.b) after irradiation and before mechanical load suggest that the matrix damage initiates more easily in the composites with higher fibre volume fractions, once the mechanical load starts to increase. However, the strength of the composites is mainly determined by matrix damage propagation, which is affected by the fibre arrangements. For $v_f = 64\%$, the uniform fibre arrangements make small increments of crack growth able to relax stress concentrations without leading to overall failure, thus moderating the effect of irradiation swelling. In contrast, for $v_f = 30\%$ and 50%, the fibre arrangements make it easier to create significant cracks, thus amplifying the effect of irradiation swelling (Fig. 11.c). When the fibre volume fraction is as low as $v_f = 10\%$, the irradiation swelling effect is less pronounced due to the insignificant amount of stress concentrations around fibres.

On the other hand, in the case of negative swelling mismatch, the residual stresses (Fig. 13.a) and the initial damage density (Fig. 14.a) suggest that the interfacial debonding is easier to occur in the composites with lower fibre volume fractions. The initial interfacial debonding makes the composites more brittle with the composite strength tending to depend solely on the matrix strength. The strength of the composites with lower v_f is less sensitive to this change (Fig. 11. c) because their intact strength is already more dependent on the matrix strength.

3.3. Effect of porosity (weak interphase composites)

Unirradiated unit cells with the same fibre volume fraction (either 30% or 64%) have been tested with different pore volume fractions: $v_p = 4\%$, $v_p = 10\%$ and $v_p = 15\%$. The simulated modulus and strength are shown in Fig. 15 as functions of pore volume

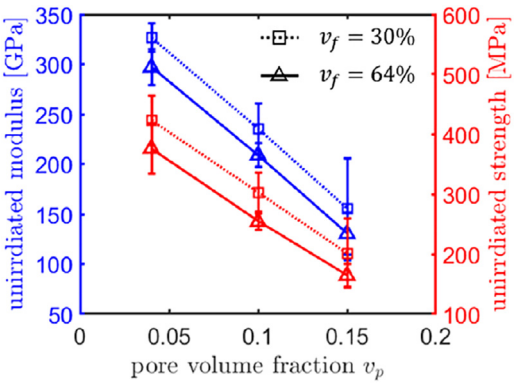

Fig. 15. Transverse elastic modulus and transverse strength of unirradiated UD composites with two different fibre densities ($v_f = 30\%$ and $v_f = 64\%$) and various pore volume fractions. The error bars are the standard deviations of the measurements from five different unit cells with the same fibre volume fraction and porosity.

fraction. Increased porosity decreases both modulus and strength. The scatter on each measurement point demonstrates that the arrangement of fibres (and their associated porosity) can affect both the strength and the elastic modulus, as already discussed in Section 3.2.1.

The macroscopic properties of unit cells with $v_f = 30\%$ and different porosities are shown in Fig. 16. Although the porosity dramatically affects the unirradiated properties, its effects on the sensitivity to irradiation swelling are small. The same conclusion can be drawn from the results for unit cells with $v_f = 64\%$ (presented in Appendix C for the sake of brevity). This is because changing the pore volume fraction over this range does not significantly change the morphology and size of pores nor the network of the PyC interphases from the fibre distribution; these two microstructural parameters have been demonstrated, from the preceding discussion, to be the key factors that determine the sensitivity of the composite's mechanical properties to irradiation swelling. Fig. 16 also implies that the observations from the previous cases with $v_p = 4\%$ should be extendable to higher pore volume fractions up to 15%.

3.4. On extrapolating the results for transverse properties

The trend analyses obtained in the present work may provide some insight into the selection of manufacturing process and process parameters of SiC/SiC composites for nuclear applications. For third generation stoichiometric fibres with CVI SiC matrix, the thermal strain mismatch is negative and in the order of magnitude of -10^{-5} (estimation based on the CTEs for HNS fibres and SiC matrix [48]). This, together with a weak PyC interphase, induces an insignificant process-induced thermal residual stress of ~30 MPa [6]. The unirradiated transverse strength and modulus both decrease with increasing fibre volume fraction (Fig. 9), so local regions of higher fibre volume fraction have lower modulus and transverse strength than regions of lower fibre volume fraction. In a braided (woven) architecture, the fibre volume fraction is highest at intersecting (or over-lapping) fibre tows. Low fibre volume fraction (higher stiffness) regions between the fibre tows experience higher stress, and the net effect is that failure tends to initiate from matrix-rich regions in the vicinity of stress concentrating pores [8]. In CVI SiC/SiC composites where a slight negative swelling mismatch ($-0.005 < s_f - s_m < 0$) most likely occurs under operating irradiation conditions in LWRs and GFRs, both modulus and transverse strength are predicted to reduce to a small extent (Fig. 11), with a somewhat greater fibre-content sensitivity for the transverse strength (Fig. 11.c) than the modulus (Fig. 11.b). Hence, in the irradiated condition the significance of stress concentrating pores in regions of lower fibre volume fraction would remain, but a propagating crack might transition more readily from the matrix-rich regions into the fibre tows (i.e. from lower to higher fibre volume fraction). This would have more detrimental consequence on the overall quasi-ductile behaviour and structural integrity if this affects extrinsic energy absorbing process such as crack deflection [7].

In comparison to the braiding technique, filament winding can produce a more uniform distribution of fibres (and porosity), for which the model suggests the overall fracture behaviour might change less with irradiation. This seems to be confirmed by the XCT observations of [24], qualitatively showing more cracks in the braided duplex composite than in the filament wound duplex composite. Integrating the outputs of the PF-CZ model into larger scale models of composite behaviour such as [49] (e.g. as the properties of representative volume elements) could allow this to be verified.

Different from the CVI process discussed above, the NITE process leads to residual tensile stresses of ~500 MPa in the matrix due to the different thermal expansions of fibres and matrix [18], i.e. NITE composites begin life with an effective positive thermal strain mismatch in the order of magnitude of 0.001. The negative swelling mismatch (i.e. greater irradiation swelling of matrix) in NITE composites under irradiation [18] should produce compressive stresses in matrix (see Fig. 12), which would compensate the thermal tensile stresses, leading to an increase in transverse strength with irradiation. This is in line with the discussion provided in [18]. The matrix swelling with irradiation is affected by the sintering additives for NITE process [50], and may thus be affected by the sintering conditions, e.g. temperature and pressure. In addition, the density and microstructure of the matrix, which may determine the thermomechanical properties of the composites, can be tailored by varying sintering conditions [51]. Models such as the one developed in this paper, with additional consideration of the afore-mentioned specificities, may be used to support the design of processing conditions of NITE-matrix composites to achieve an optimal balance of thermal residual stress and irradiation swelling for high strength composites.

3.5. Illustrative results for longitudinal behaviour

To demonstrate the capability of the proposed PF-CZ model, we provide some results for longitudinal behaviour of unidirectional composites. First, some 3D periodic unit cells with different fibre volume fractions will be analysed and the potential effect of swelling mismatch will be illustrated. Then, a mini-composite structure will be simulated and its longitudinal properties compared with the experimental results from the literature. These numerical examples are given herein for illustrative purpose, showing how experiment data can be used to tune model parameters; a detailed investigation of longitudinal behaviour merits a separate paper.

3.5.1. Three-dimensional periodic unit cells

For these simulations, the material parameters were kept the same as previously, except the fracture property for the fibres. We assign the fibres with a fracture toughness of 2.1 N/mm, which is calculated from $G_c = 256 l_c \sigma_c^2 / 27E$ (see [33] for the demonstration of this formula), where $l_c = 0.002$ mm (same as the value for matrix), $E = 365$ GPa and $\sigma_c = 6.4$ GPa measured by [38]. Three unit cells with different fibre volume fractions are tested. A matrix notch is created to introduce the flaw for crack initiation, as shown in Fig. 17.

The macroscopic curves of three unit cells with different fibre volume fractions are shown in Fig. 18.a. It is worth noting that the irreversibility of bulk damage was enforced by forbidding the damage variable to decrease. This helped remove the oscillating peaks

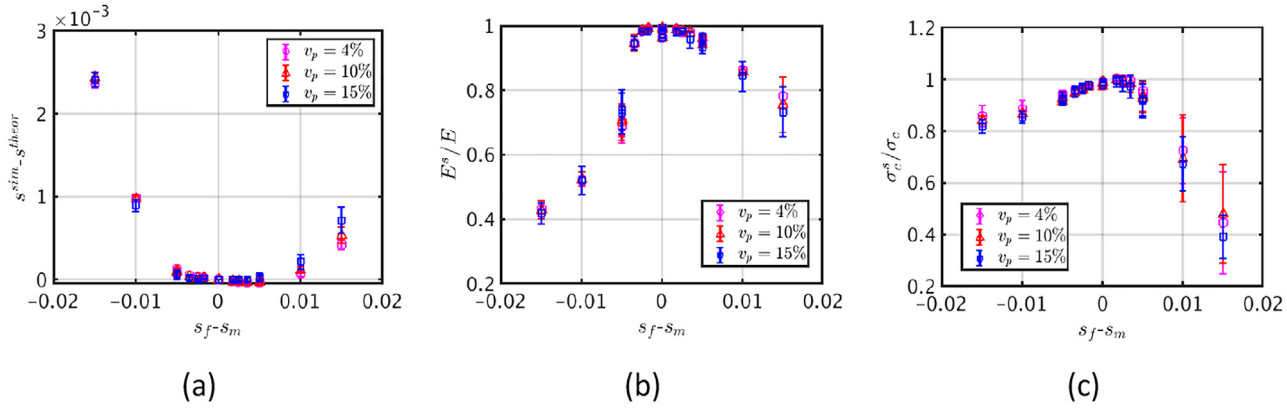

Fig. 16. Property changes induced by swelling mismatch for unit cells with the same fibre volume fraction ($v_f = 30\%$) and different pore volume fractions: (a) over-swelling, (b) degradation in transverse elastic modulus, (c) degradation in transverse strength.

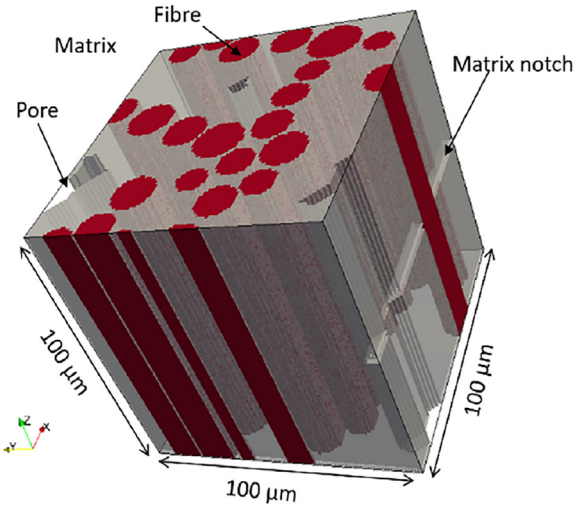

Fig. 17. A 3D unit cell used for the study of longitudinal behaviour of UD composites ($v_f = 30\%$, $v_p = 4\%$). To introduce a flaw for crack initiation, a notch was created in the matrix. For the same of visibility matrix voxels have been set to be semi-transparent and pore voxels are hidden.

in the stress-strain curves observed in [26] (see Appendix D). The stress-strain curves for smaller fibre volume fractions ($v_f = 10\%$ and $v_f = 30\%$) exhibit an early damage onset and more dramatic drops of stress at damage onset. This is because a larger fibre volume fraction causes the load to be shared more uniformly, thus preventing sudden load transfer from matrix to fibres.

Damage growth in each phase (fibres, matrix and interphase) at different loading steps are shown in Fig. 18.b for each unit cell. In general, matrix cracks propagate accompanied by interphase degradation. Multiple parallel matrix cracks are created at the late loading steps. Comparing the crack patterns at the last step, the effect of fibre volume fraction is observed: a larger v_f seems to generate smaller spacing of matrix cracks. This could be related to the more uniformly shared load in the composites with higher fibre volume fractions, which also explains the difference in stress-strain behaviour that was noted in the previous paragraph. Furthermore, although no fibre breakage (damage variable close to 1) were predicted in the simulations, quite significant damage can be observed in fibres at the last loading step. It must be noted that the modelling strategy adopted herein is based on continuum damage mechanics, which smears brittle fracture into a diffuse damage field.

The effects of swelling mismatch on the longitudinal behaviour are illustrated in Fig. 19. Comparing to the no-swelling situation, the onset of the nonlinearity of the stress-strain curve increases for the negative swelling mismatch ($s_m = 0.01$, $s_f = 0.005$), and decreases for the positive mismatch ($s_m = 0.01$, $s_f = 0.015$). The damage patterns are shown for each case at similar loading strains. Multiple parallel matrix cracks appear in all the situations and the negative mismatch seems to induce a larger crack spacing than the positive mismatch. This difference should be produced via the change in the initial interphase state (residual stress and damage) that is induced by the swelling mismatch (see Section 3.2.3). However, one should remain cautious when extrapolating this numerical example to possible experimental conditions, as the initial interphase properties (fracture and friction) might be not representative. These parameters have been taken from some experimental measurements in the literature, but they may exhibit large discrepancies due to the technical challenges of their measurement. Nonetheless, the simulation shows that swelling mismatch has the potential to affect the longitudinal properties of the composite.

3.5.2. Damage behaviour of a mini-composite compared to experiment

To verify the potential of the damage modelling framework to accurately simulate experimental behaviour, four simulations were conducted on a mini-composite structure (Fig. 20.b) using different material parameters for fibres, matrix and interphase (Table 1). This virtually generated mini-composite mimics the real structure observed in [13], which exhibits a non-uniform distribution of matrix (Fig. 20.a). The domain contains 263 fibres and is discretised with 27 million voxels (elements). Note that the real mini-composite shown in Fig. 20.a contains around 500 fibres. However, the present work aims to demonstrate the capability of the model, so a smaller number of fibres (still ensuring a similar porosity of 15% and a similar fibre volume fraction ~50%) were used to reduce the computation cost. The simulations were performed using 2 compute nodes (48 cores per node). Each simulation took 7 – 12 h to run before they were stopped due to the allocated CPU time reaching the limits.

The material parameters have been manually tuned to fit the macroscopic stress-strain curves to the experimental measurement, as shown in Fig. 20.c. A more rigorous parameter identification can be conducted, but that is beyond the scope of the present paper. The predicted elastic moduli are in good agreement with the experiment for all simulations. Simulation M4, representing weak interphase, and a slight reduction in matrix strength, fits the experimental data well.

The damage growth for the simulation M4 is shown in Fig. 21. The model was able to capture the complex interactions between matrix cracking and interphase fracture. The damage starts from

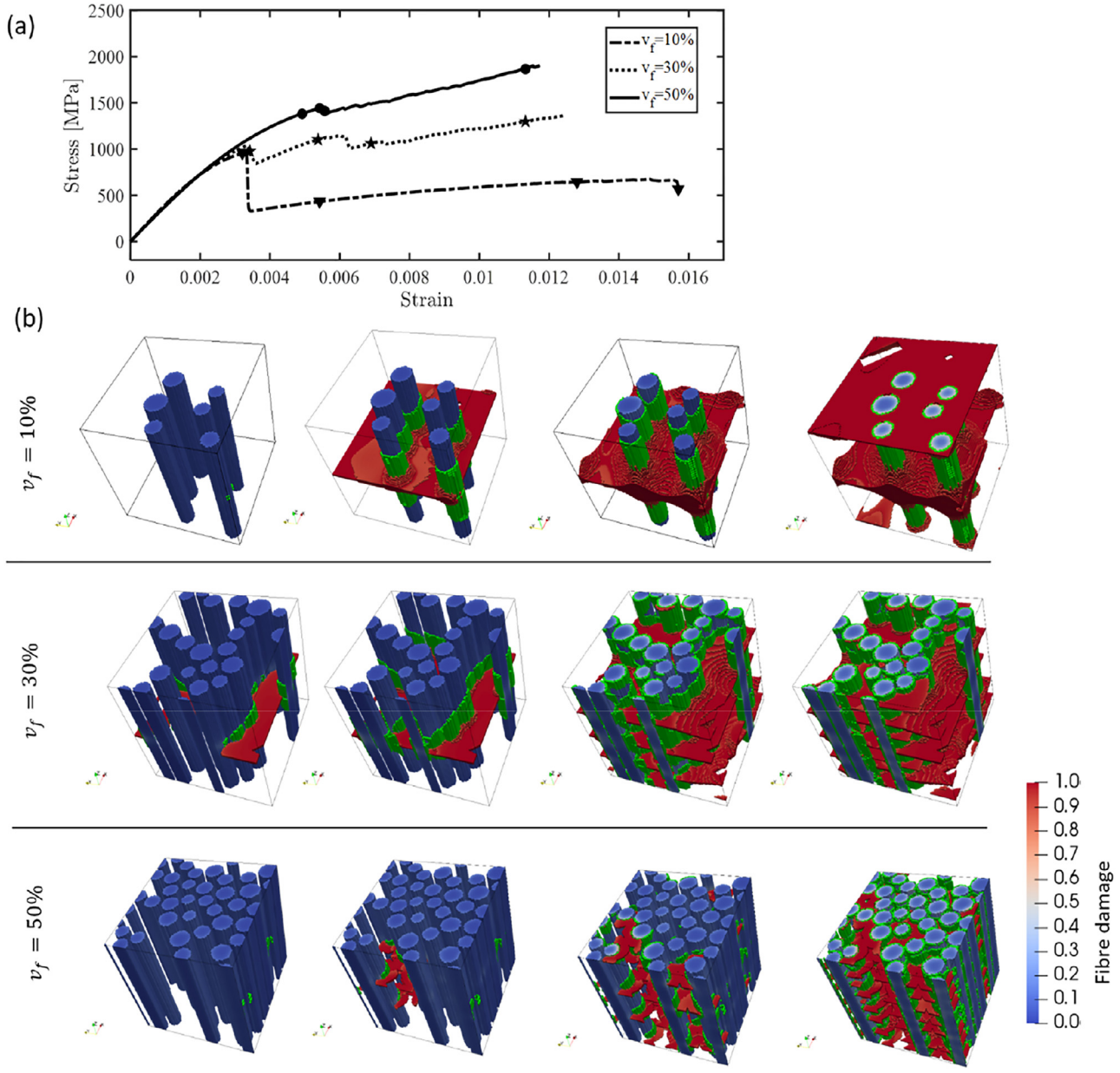

Fig. 18. (a) Stress-strain curves of three unit cells with different v_f and the same $v_p = 4\%$, under longitudinal tension. The markers (triangle, pentagram and disk) indicate the loading steps at which damage patterns shown in (b). (b) Damage growth in the three unit cells: matrix damage ($d > 0.9$) shown in red and interphase damage ($d^I > 0.9$) shown in green, whereas full range of fibre damage shown as indicated by the colour bar.

Table 1
Material properties used for the mini-composite simulations.

	M1	M2	M3	M4
Fibre	$G_c = 0.5$ N/mm $l_c = 0.002$ mm	$G_c = 0.5$ N/mm $l_c = 0.002$ mm	$G_c = 0.5$ N/mm $l_c = 0.001$ mm	$G_c = 0.5$ N/mm $l_c = 0.001$ mm
Matrix	$G_c = 0.01$ N/mm $l_c = 0.002$ mm	$G_c = 0.01$ N/mm $l_c = 0.002$ mm	$G_c = 0.008$ N/mm $l_c = 0.002$ mm	$G_c = 0.008$ N/mm $l_c = 0.002$ mm
Interphase	$\sigma_{cI/cII} = 300$ MPa $G_{cI/cII} = 0.002$ MPa $\mu = 0.1$	$\sigma_{cI/cII} = 50$ MPa $G_{cI/cII} = 0.002$MPa $\mu = 0.1$	$\sigma_{cI/cII} = 300$ MPa $G_{cI/cII} = 0.002$MPa $\mu = 0.25$	$\sigma_{cI/cII} = 50$ MPa $G_{cI/cII} = 0.002$MPa $\mu = 0.25$

the outer surface, where a tiny crack (~3 μm notching into the peripheral matrix) was pre-defined. Then, the damage propagates in both the radial and the circumferential directions, and there is a tendency of a helical propagation path to be observed in the last loading step. These damage growth trends are consistent with the experimental observations of [13]. The crack spacing close to the initialisation site is around 60 μm, which is lower than the value of ~200 μm observed from the in-situ SEM experiment [13]. This might be due to the periodicity of the numerical model in boundary conditions and microstructure along the longitudinal direction, and a simulation with longer mini-composites may provide better predictions of the crack spacing.

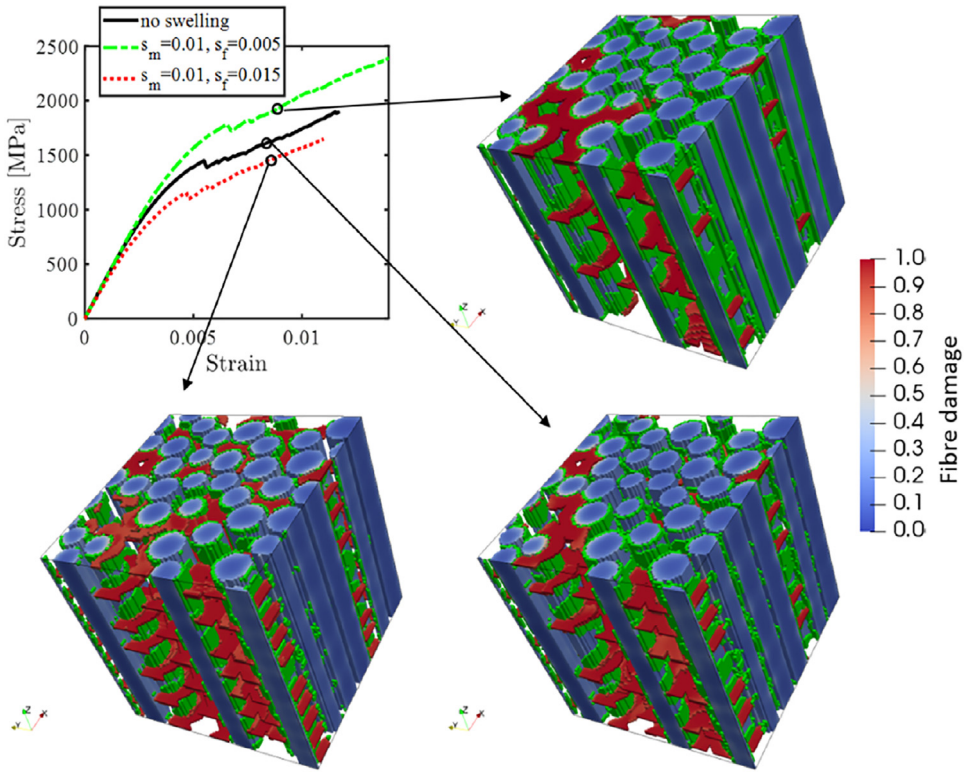

Fig. 19. Effect of swelling mismatch on the longitudinal behaviour of the UD composite with $v_f = 50\%$ and $v_p = 4\%$. The stress-strain curves for irradiated composites have been shifted to the origin by subtracting an offset, which is the swelling strain induced by irradiation.

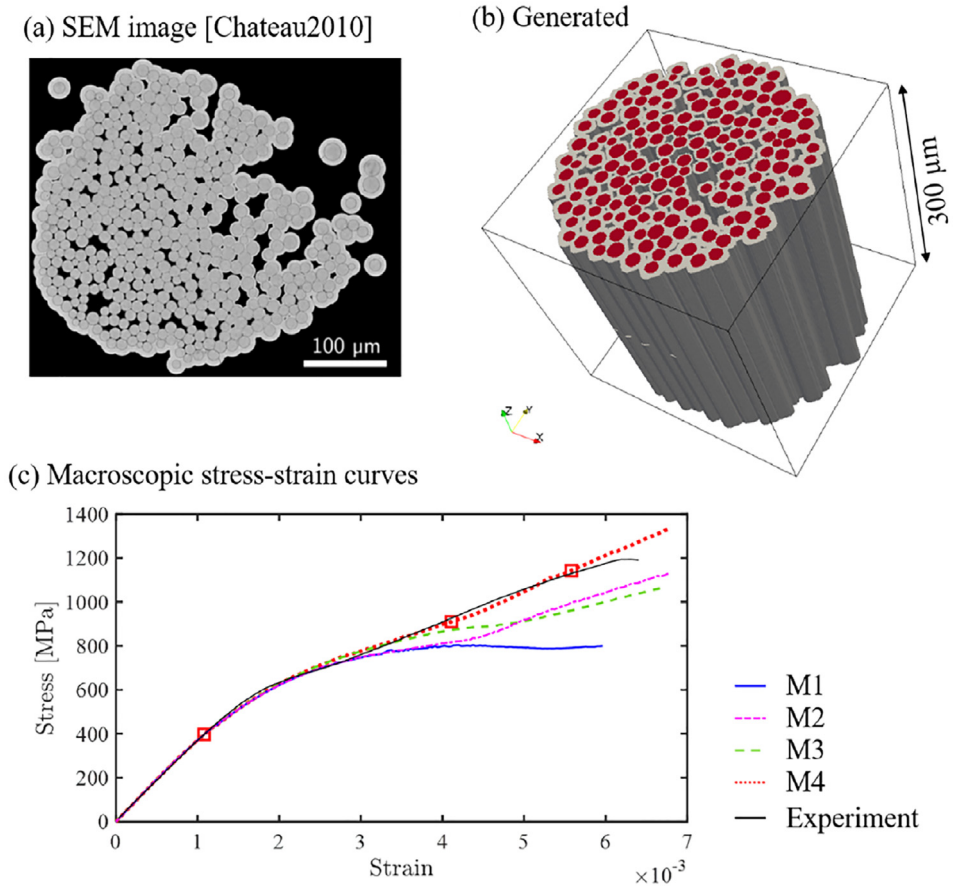

Fig. 20. Mini-composite simulations: (a) cross-section of a mini-composite studied by Chateau (2010) [13]; (b) a virtually generated mini-composite structure; (c) macroscopic stress-strain curves from the FFT simulations, compared to the experiment of [13], where the red squares correspond to the three loading steps that are visualised in Fig. 21.

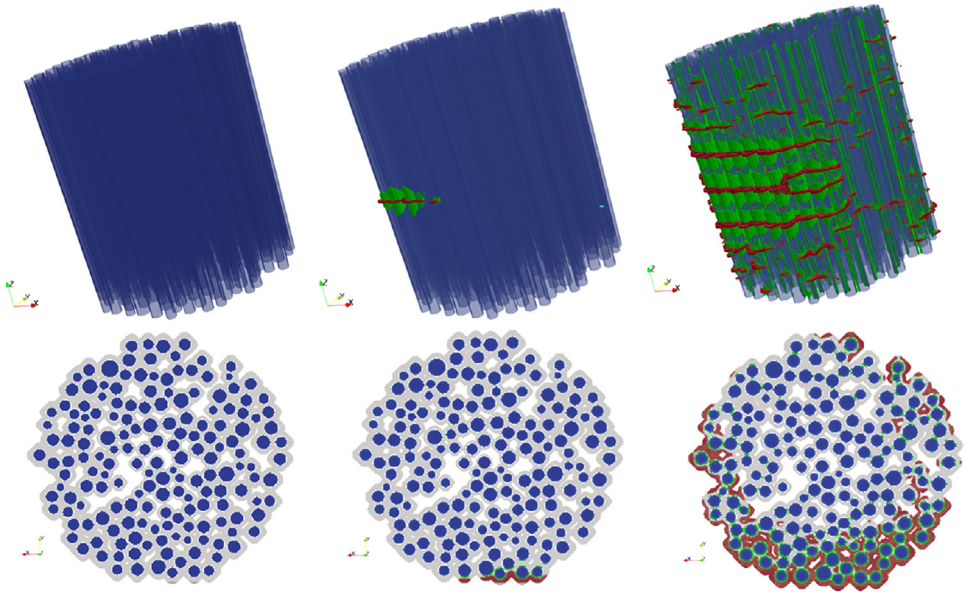

Fig. 21. Damage growth in the mini-composite simulated using M4 parameters (Table 1). From left to right correspond to the three loading steps indicated by the red squares in Fig. 20. First row – 3D view, second row – 2D plane view. Green shows interphase fracture and red shows matrix cracks.

4. Summary

Using a continuum damage model, the predicted effects of irradiation swelling of the SiC matrix and fibres on mechanical properties of UD SiC/SiC composites have been studied. The objective of the present work is to perform an elementary mechanistic analysis on one of the irradiation effects – swelling, and not to accurately predict the behaviour of a particular SiC/SiC composite under a given irradiation condition. This mechanistic analysis provides some guidelines for characterising the swelling behaviour at microstructural level. The focus has been placed on transverse properties, with some illustrative 3D studies of longitudinal properties.

A large number of simulations were conducted to analyse the transverse properties and the changes induced by swelling mismatch between fibres and matrix. The swelling mismatch, instead of the absolute values, is the dominant factor in the degradation of the transverse mechanical properties. Residual tensile stresses are created in the fibres for negative swelling mismatch ($s_f < s_m$) and in the matrix for positive mismatch ($s_f > s_m$). A strong interphase makes the transverse modulus and strength of the composites insensitive to negative swelling mismatch, whereas a weak interphase produces a better tolerance to positive mismatch on the strength of the composite. The fibre volume fraction affects not only the initial properties of unirradiated composites, but also the sensitivity to irradiation swelling. The volume fraction of fibres can significantly affect the transverse modulus and strength of the composites. High fibre volume fraction (~30% to 50%) can produce a network of weak interphases, large stress concentrating pores that result in lower initial transverse modulus and strength, and also a higher sensitivity of the transverse properties to irradiation swelling. Nevertheless, when the fibre volume fraction reaches a certain level (e.g. 64%), the distribution of fibres becomes relatively uniform due to closer packing. This prevents the formation of large pores, and produces a slightly higher transverse modulus and strength and a lower sensitivity to irradiation swelling. The pore volume fraction has a strong effect on the unirradiated transverse properties, but has a minor effect on the sensitivity to irradiation swelling.

Illustrative 3D examples for the longitudinal behaviour of the UD composites have revealed that the spacing of the matrix cracks may be affected by both fibre volume fraction (through load sharing between fibres and matrix) and swelling mismatch (changing the interphase state of residual stress and damage). Through the comparison with experimental observations for non-irradiated mini-composites, the model have been proven to be capable of predicting the pseudo-ductile stress-strain curves together with the complex multiphasic cracking at microscopic level.

Finally, we highlight some potential limitations and point to some necessary future work. First, reliable experimental data for irradiated SiC/SiC are critical, and when these become available, it will be possible to tune the model parameters, with the expectation of simulating stress-strain curves that are comparable to those experiments. Second, in-service performance of SiC/SiC composites is also affected by physics other than swelling, such as creep [1]. To obtain an accurate in-service prediction, these phenomena need to be included into the modelling framework, which is capable of accommodating this additional complexity. The swelling of PyC interphase has not been considered in this study. This simplification can be rationalised by the low elastic modulus (25 GPa) and small thickness (in the order of 100 nm) of the interphase layer, which together with the expected relaxation by irradiation creep will limit its effect on the stress field. Nonetheless, the current framework can be readily adapted for investigation on the effects of interphase swelling, which may be more important for composites with multilayer PyC-SiC or a thicker PyC interphase. It should be noted that although the thickness of the interphase is not explicitly considered in the proposed model, its effect can be represented by changing the effective strength of the interphase.

5. Conclusions

A microscale model has been developed to simulate the mechanical behaviour of irradiated fibre composites, including matrix cracking and interface debonding. It has been applied to investigate the potential effects of swelling mismatch between fibres and matrix on the transverse and longitudinal tensile mechanical properties of unidirectional SiC/SiC composites with various fibre contents and porosities.

The sensitivity of the composites' mechanical properties to irradiation swelling was affected by the fibre volume fraction. It was not affected by the pore volume fraction, though the porosity dramatically affected the initial unirradiated properties. This may lead to heterogeneity in damage development in composites with more complex architectures, and different sensitivity to irradiation effects between different architectures such as braided or filament wound composites.

The material parameters in the modelling framework can be tuned by simulation of mechanical experiments, and it has the potential to address changes in the properties of the interphase between fibre and matrix.

Declaration of Competing Interest

The authors declare that they have no known competing financial interests or personal relationships that could have appeared to influence the work reported in this paper.

CRediT authorship contribution statement

Yang Chen: Conceptualization, Data curation, Formal analysis, Investigation, Methodology, Software, Validation, Writing – original draft, Writing – review & editing. **James Marrow:** Writing – review & editing, Project administration, Resources, Supervision.

Data Availability

Data will be made available on request.

Acknowledgement

This project has received funding from the Euratom research and training programme 2014-2018 under grant agreement No 740415 (ll Trovatore). The authors would like to acknowledge the use of the University of Oxford Advanced Research Computing (ARC) facility in carrying out this work.

Appendix

Appendix A. Total swelling of the UD composites at different swelling mismatches

Table 1 shows the predicted total swelling of the weak-interphase composites with different fibre volume fractions at various swellings. We recall that these predicted total swellings are similar as the theoretical values calculated by the formula introduced in Section 3.1.3 (small over-swelling). The values in this table are in the same order of the experimental values found in the literature for different types of SiC/SiC composites, see e.g. [21,22,44].

Irradiation temperature	v_f	γ=-1.5	γ=-0.5	γ=-0.25	γ=0	γ=0.25	γ=0.5	γ=1.5
300 °C	**10%**	-	0.0197	0.0195	0.02	0.0205	0.0211	-
(s_m=0.02)	**30%**	-	0.0181	0.0185	0.02	0.0216	0.0233	-
	50%	-	0.0157	0.0174	0.02	0.0227	0.0255	-
	64%	-	0.0137	0.0167	0.02	0.0234	0.0269	-
500 °C	**10%**	0.0098	0.0096	0.0097	0.01	0.0103	0.0105	0.0116
(s_m=0.01)	**30%**	0.0084	0.0085	0.0092	0.01	0.0108	0.0116	0.0152
	50%	0.0057	0.0074	0.0087	0.01	0.0113	0.0127	0.0188
	64%	0.0021	0.0067	0.0083	0.01	0.0117	0.0134	0.0209
800 °C	**10%**	-	0.0067	0.0068	0.007	0.0072	0.0074	-
(s_m=0.007)	**30%**	-	0.0059	0.0065	0.007	0.0076	0.0081	-
	50%	-	0.0052	0.0061	0.007	0.0079	0.0089	-
	64%	-	0.0047	0.0058	0.007	0.0082	0.0093	-

Table 1. Predicted total swelling of the weak-interphase composites irradiated at different temperatures, with different fibre volume fractions and different relative swellings of fibres $s_f = (1+\gamma)s_m$.

Appendix B. Damage field of the unit cells with different fibre volume fractions

Fig. B.1 shows example maps of the damage induced by different swelling mismatches of the composites with different fibre volume fractions. From the second column ($s_f - s_m = -0.005$), one can observe that the proportion of interfacial damage increases as the fibre volume fraction decreases. This is quantified in the trend shown in Fig. 14.a. In the fourth column ($s_f - s_m = 0.015$), it can be seen that the highest fibre volume fraction ($v_f = 64\%$) has a more uniform distribution of the damage field, which is qualitatively different from the

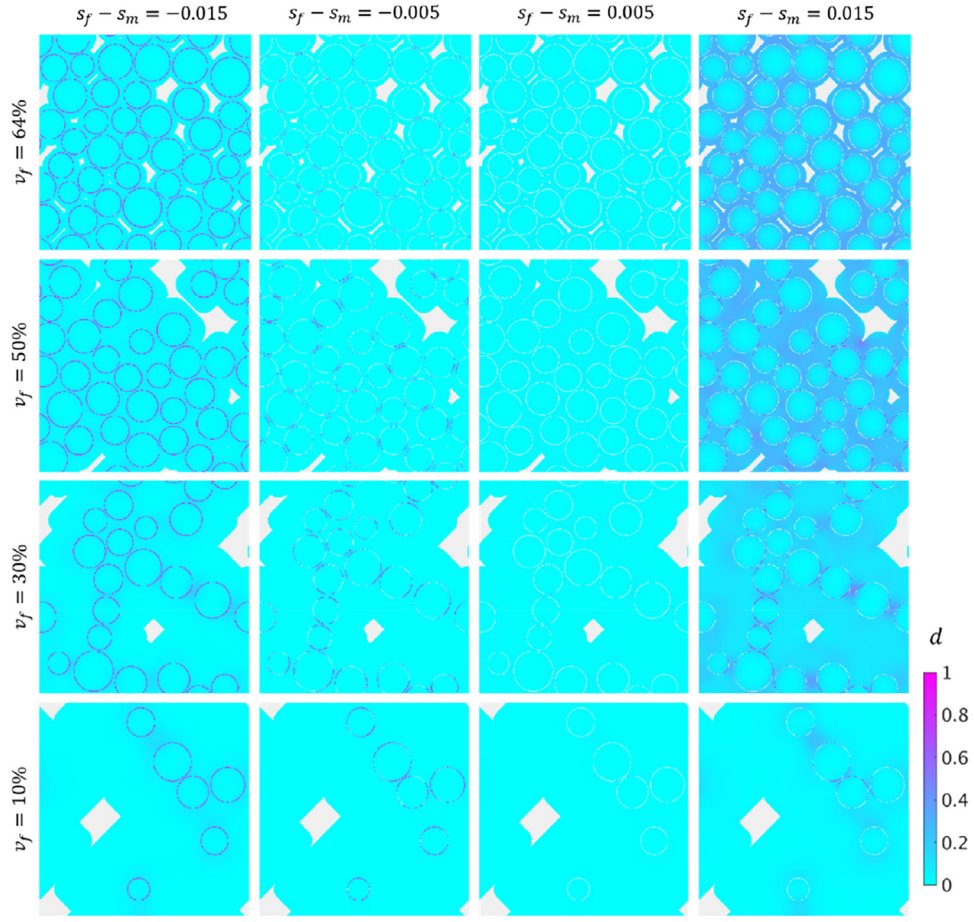

Fig. B.1. Maps of damage induced by different swelling mismatches of the composites with the same porosity ($v_p = 4\%$) and different fibre volume fractions.

lower fibre volume fractions. Also, it should be noted that marked damage occurs at the pore edges for $v_f = 50\%$, which is in agreement with the concentrated stresses observed in Fig. 12.

Appendix C. Effect of porosity on the sensitivity to irradiation swelling for composites with $v_f = 64\%$

It can be seen from Fig. C.1 that the pore volume fraction has a slight effect on the sensitivity to irradiation swelling.

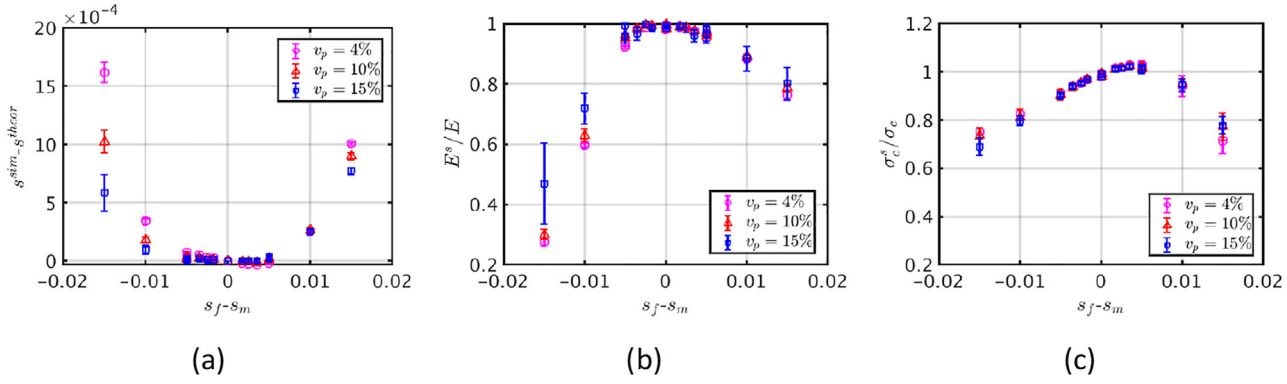

Fig. C.1. Property changes induced by swelling mismatch for unit cells with the fibre volume fraction of $v_f = 64\%$ and different pore volume fractions: (a) over-swelling, (b) degradation in elastic modulus, (c) degradation in transverse strength.

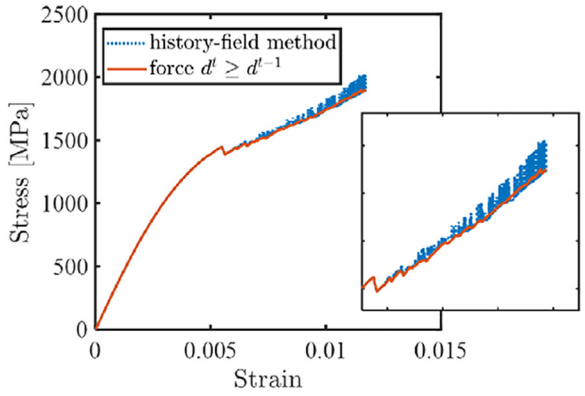

Fig. D.1. Stress-strain curves of a UD composite unit cell with $v_f = 50\%$ and $v_p = 4\%$ under longitudinal tension, no swelling. Two different methods were used to enforce the irreversibility of bulk damage: history-field method (blue curve) or direct constraint $d^t \geq d^{t-1}$ (orange curve).

Appendix D. Oscillations in stress-strain curves due to insufficient enforcement of damage irreversibility

In our previous work [26], the irreversibility of bulk damage variable was taken into account by using the history-field method proposed by Miehe et al. [27]. Although no issue was encountered for the transverse loading, strong oscillations in the stress-strain curves were observed for longitudinal loading, as shown in Fig. D.1. By examining the damage fields at the oscillating peaks, decreasing bulk damage was found at these loading steps. Therefore, we enforced the irreversibility by directly constraining the damage variable to monotonously increase, i.e. $d^t \geq d^{t-1}$. This modification allows the oscillations in the stress-strain curve to be removed as shown in Fig. D.1.

References

[1] Y. Katoh, K. Ozawa, C. Shih, T. Nozawa, R.J. Shinavski, A. Hasegawa, et al., Continuous SiC fiber, CVI SiC matrix composites for nuclear applications: properties and irradiation effects, J. Nucl. Mater. 448 (2014) 448–476, doi:10.1016/j.jnucmat.2013.06.040.

[2] S.J. Zinkle, K.A. Terrani, J.C. Gehin, L.J. Ott, L.L. Snead, Accident tolerant fuels for LWRs: a perspective, J. Nucl. Mater. 448 (2014) 374–379, doi:10.1016/j.jnucmat.2013.12.005.

[3] L.L. Snead, T. Nozawa, T.S. Byun, S. Kondo, D.A. Petti, Handbook of SiC properties for fuel performance modeling, J. Nucl. Mater. 371 (2007) 329–377.

[4] L.L. Snead, T. Nozawa, M. Ferraris, Y. Katoh, R. Shinavski, M. Sawan, Silicon carbide composites as fusion power reactor structural materials, J. Nucl. Mater. 417 (2011) 330–339, doi:10.1016/j.jnucmat.2011.03.005.

[5] F. Bernachy-Barbe, L. Gélébart, M. Bornert, J. Crépin, C. Sauder, Anisotropic damage behavior of SiC/SiC composite tubes: multiaxial testing and damage characterization, Compos. Part A Appl. Sci. Manuf. 76 (2015) 281–288, doi:10.1016/j.compositesa.2015.04.022.

[6] J. Braun, C. Sauder, J. Lamon, F. Balbaud-Célérier, Influence of an original manufacturing process on the properties and microstructure of SiC/SiC tubular composites, Compos. Part A Appl. Sci. Manuf. 123 (2019) 170–179.

[7] Y. Chen, L. Gélébart, C. Chateau, M. Bornert, A. King, C. Sauder, et al., Crack initiation and propagation in braided SiC/SiC composite tubes: effect of braiding angle, J. Eur. Ceram. Soc. 40 (2020) 4403–4418, doi:10.1016/j.jeurceramsoc.2020.04.060.

[8] Y. Chen, L. Gélébart, C. Chateau, M. Bornert, C. Sauder, A. King, Analysis of the damage initiation in a SiC/SiC composite tube from a direct comparison between large-scale numerical simulation and synchrotron X-ray microcomputed tomography, Int. J. Solids Struct. 161 (2019) 111–126, doi:10.1016/j.ijsolstr.2018.11.009.

[9] Y. Chen, L. Gélébart, C. Chateau, M. Bornert, A. King, P. Aimedieu, et al., 3D detection and quantitative characterization of cracks in a ceramic matrix composite tube using X-ray computed tomography, Exp. Mech. 60 (2020) 409–424, doi:10.1007/s11340-019-00557-5.

[10] G.N. Morscher, Stress-dependent matrix cracking in 2D woven SiC-fiber reinforced melt-infiltrated SiC matrix composites, Compos. Sci. Technol. 64 (2004) 1311–1319, doi:10.1016/j.compscitech.2003.10.022.

[11] C. Simon, F. Rebillat, V. Herb, G. Camus, Monitoring damage evolution of SiCf/[SiBC]m composites using electrical resistivity: crack density-based electromechanical modeling, Acta Mater. 124 (2017) 579–587, doi:10.1016/j.actamat.2016.11.036.

[12] F. Bernachy-Barbe, L. Gélébart, M. Bornert, J. Crépin, C. Sauder, Characterization of SiC/SiC composites damage mechanisms using digital image correlation at the tow scale, Compos. Part A Appl. Sci. Manuf. 68 (2015) 101–109, doi:10.1016/j.compositesa.2014.09.021.

[13] C. Chateau, L. Gélébart, M. Bornert, J. Crépin, E. Boller, C. Sauder, et al., *In situ* X-ray microtomography characterization of damage in SiCf/SiC minicomposites, Compos. Sci. Technol. 71 (2011) 916–924, doi:10.1016/j.compscitech.2011.02.008.

[14] H.A. Bale, A. Haboub, A.A. Macdowell, J.R. Nasiatka, D.Y. Parkinson, B.N. Cox, et al., Real-time quantitative imaging of failure events in materials under load at temperatures above 1600°C, Nat. Mater. 12 (2013) 40–46, doi:10.1038/nmat3497.

[15] V. Mazars, O. Caty, G. Couégnat, A. Bouterf, S. Roux, S. Denneulin, et al., Damage investigation and modeling of 3D woven ceramic matrix composites from X-ray tomography *in-situ* tensile tests, Acta Mater. 140 (2017) 130–139, doi:10.1016/j.actamat.2017.08.034.

[16] T. Nozawa, Y. Katoh, L.L. Snead, The effect of neutron irradiation on the fiber/matrix interphase of silicon carbide composites, J. Nucl. Mater. 384 (2009) 195–211, doi:10.1016/j.jnucmat.2008.11.015.

[17] T. Nozawa, T. Koyanagi, Y. Katoh, H. Tanigawa, High-dose, intermediate-temperature neutron irradiation effects on silicon carbide composites with varied fiber/matrix interfaces, J. Eur. Ceram. Soc. 39 (2019) 2634–2647, doi:10.1016/j.jeurceramsoc.2019.03.014.

[18] T. Koyanagi, S. Kondo, T. Hinoki, Effect of differential swelling between fiber and matrix on the strength of irradiated SiC/SiC composites, J. Nucl. Mater. 442 (2013) S380–S383.

[19] S. Kondo, T. Hinoki, M. Nonaka, K. Ozawa, Irradiation-induced shrinkage of highly crystalline SiC fibers, Acta Mater. 83 (2015) 1–9.

[20] S. Agarwal, G. Duscher, Y. Zhao, M.L. Crespillo, Y. Katoh, W.J. Weber, Multiscale characterization of irradiation behaviour of ion-irradiated SiC/SiC composites, Acta Mater. 161 (2018) 207–220, doi:10.1016/j.actamat.2018.09.012.

[21] G. Newsome, L.L. Snead, T. Hinoki, Y. Katoh, D. Peters, Evaluation of neutron irradiated silicon carbide and silicon carbide composites, J. Nucl. Mater. 371 (2007) 76–89.

[22] L.L. Snead, Y. Katoh, A. Kohyama, J.L. Bailey, N.L. Vaughn, R.A. Lowden, Evaluation of neutron irradiated near-stoichiometric silicon carbide fiber composites, J. Nucl. Mater. 283–287 (2000) 551–555, doi:10.1016/S0022-3115(00)00235-X.

[23] G. Singh, T. Koyanagi, C. Petrie, K. Terrani, Y. Katoh, Evaluating the irradiation effects on the elastic properties of miniature monolithic SiC tubular specimens, J. Nucl. Mater. 499 (2018) 107–110.

[24] J.D. Arregui-Mena, T. Koyanagi, E. Cakmak, C.M. Petrie, W.J. Kim, D. Kim, et al., Qualitative and quantitative analysis of neutron irradiation effects in SiC/SiC composites using X-ray computed tomography, Compos. Part B Eng. 238 (2022) 109896.

[25] C. Chateau Analyse expérimentale et modélisation micromécaniques du comportement élastique et de l'endommagement de composites SiC/SiC unidirectionnels. Ecole polytechnique, 2011.

[26] Y. Chen, L. Gélébart, A. Marano, T.J. Marrow, FFT phase-field model combined with cohesive composite voxels for fracture of composite materials with interfaces, Comput. Mech. 68 (2021) 433–457, doi:10.1007/s00466-021-02041-1.

[27] C. Miehe, M. Hofacker, F. Welschinger, A phase field model for rate-independent crack propagation: robust algorithmic implementation based on operator splits, Comput. Methods Appl. Mech. Eng. 199 (2010) 2765–2778, doi:10.1016/j.cma.2010.04.011.

[28] G. Alfano, E. Sacco, Combining interface damage and friction in a cohesive-zone model, Int. J. Numer. Methods Eng. 68 (2006) 542–582, doi:10.1002/nme.1728.

[29] Y. Chen, D. Vasiukov, L. Gélébart, C. Park, A FFT solver for variational phase-field modeling of brittle fracture, Comput. Methods Appl. Mech. Eng. 349 (2019) 167–190, doi:10.1016/J.CMA.2019.02.017.

[30] T. Kanit, S. Forest, I. Galliet, V. Mounoury, D. Jeulin, Determination of the size of the representative volume element for random composites: statistical and numerical approach, Int. J. Solids Struct. 40 (2003) 3647–3679, doi:10.1016/S0020-7683(03)00143-4.

[31] L. Gélébart, F. Ouaki, Filtering material properties to improve FFT-based methods for numerical homogenization, J. Comput. Phys. 294 (2015) 90–95, doi:10.1016/j.jcp.2015.03.048.

[32] M. Kabel, D. Merkert, M. Schneider, Use of composite voxels in FFT-based homogenization, Comput. Methods Appl. Mech. Eng. 294 (2015) 168–188, doi:10.1016/j.cma.2015.06.003.

[33] T.T. Nguyen, J. Yvonnet, M. Bornert, C. Chateau, K. Sab, R. Romani, et al., On the choice of parameters in the phase field method for simulating crack initiation with experimental validation, Int. J. Fract. 197 (2016) 213–226, doi:10.1007/s10704-016-0082-1.

[34] T. Hinoki, L.L. Snead, Y. Katoh, A. Hasegawa, T. Nozawa, A. Kohyama, The effect of high dose/high temperature irradiation on high purity fibers and their silicon carbide composites, J. Nucl. Mater. 307 (2002) 1157–1162.

[35] M. Ben-Belgacem, V. Richet, K.A. Terrani, Y. Katoh, L.L. Snead, Thermo-mechanical analysis of LWR SiC/SiC composite cladding, J. Nucl. Mater. 447 (2014) 125–142.

[36] Y. Katoh, T. Nozawa, C. Shih, K. Ozawa, T. Koyanagi, W. Porter, et al., High-dose neutron irradiation of Hi-Nicalon Type S silicon carbide composites. Part 2: mechanical and physical properties, J. Nucl. Mater. 462 (2015) 450–457.

[37] Y. Katoh, L.L. Snead, T. Nozawa, S. Kondo, J.T. Busby, Thermophysical and mechanical properties of near-stoichiometric fiber CVI SiC/SiC composites after neutron irradiation at elevated temperatures, J. Nucl. Mater. 403 (2010) 48–61, doi:10.1016/j.jnucmat.2010.06.002.
[38] Y. Zayachuk, P. Karamched, C. Deck, P. Hosemann, A. D.E, Linking microstructure and local mechanical properties in SiC-SiC fiber composite using micromechanical testing, Acta Mater. 168 (2019) 178–189.
[39] R.J. Price, Effects of fast-neutron irradiation on pyrolytic silicon carbide, J. Nucl. Mater. 33 (1969) 17–22.
[40] Y. Katoh, L.L. Snead, Silicon carbide and its composites for nuclear applications–historical overview, J. Nucl. Mater. 526 (2019) 151849.
[41] P. Hosemann, J. Tucker, D. Cahill Developing a macro-scale SiC-cladding behavior model based on localized mechanical and thermal property evaluation on pre-and post-irradiation SiC-SiC composites. University of California, Berkeley, CA (United States): 2019.
[42] Y. Katoh, P. Bansal, J. Lamon, Radiation effects, in: Ceramic Matrix Composites: Materials, Modeling and Technology, John Wiley & Sons, Incorporated, 2014, pp. 389–404.
[43] L.P. Zawada, R.S. Hay, S.S. Lee, J. Staehler, Characterization and high-temperature mechanical behavior of an oxide/oxide composite, J. Am. Ceram. Soc. 86 (2003) 981–990.
[44] Y. Katoh, T. Koyanagi, J.L. McDuffee, L.L. Snead, K. Yueh, Dimensional stability and anisotropy of SiC and SiC-based composites in transition swelling regime, J. Nucl. Mater. 499 (2018) 471–479.
[45] C. Chateau, L. Gélébart, M. Bornert, J. Crépin, Micromechanical modeling of the elastic behavior of unidirectional CVI SiC /SiC composites, Int. J. Solids Struct. 58 (2015) 322–334, doi:10.1016/j.ijsolstr.2014.11.020.
[46] I. Sevostianov, A. Giraud, On the compliance contribution tensor for a concave superspherical pore, Int. J. Fract. 177 (2012) 199–206.
[47] Y. Vertyagina, T.J. Marrow, A multi-scale three-dimensional Cellular Automata fracture model of radiolytically oxidised nuclear graphite, Carbon NY 121 (2017) 574–590.
[48] E. Buet, C. Sauder, D. Sornin, S. Poissonnet, J.N. Rouzaud, C. Vix-Guterl, Influence of surface fibre properties and textural organization of a pyrocarbon interphase on the interfacial shear stress of SiC/SiC minicomposites reinforced with Hi-Nicalon S and Tyranno SA3 fibres, J. Eur. Ceram. Soc. 34 (2014) 179–188, doi:10.1016/j.jeurceramsoc.2013.08.027.
[49] L. Saucedo-Mora, T.J. Marrow, Multi-scale damage modelling in a ceramic matrix composite using a finite-element microstructure meshfree methodology, Philos. Trans. R. Soc. A Math. Phys. Eng. Sci. 374 (2016) 20150276.
[50] T. Koyanagi, S. Kondo, T. Hinoki, The influence of sintering additives on the irradiation resistance of NITE SiC, J. Nucl. Mater. 417 (2011) 435–439, doi:10.1016/j.jnucmat.2010.12.181.
[51] Y. Katoh, S. Dong, A. Kohyama, Thermo-mechanical properties and microstructure of silicon carbide composites fabricated by nano-infiltrated transient eutectoid process, Fusion Eng. Des. 61–62 (2002) 723–731.